

A Thesis

entitled

Recovering skin conductance responses in under-sampled
electrodermal activity data from wearables

by

Abhishek Mukherjee

Submitted to the Graduate Faculty as partial fulfillment of the requirements for the
Masters of Science Degree in Computer Science

Dr. Kevin S. Xu, Committee Chair

Dr. Qin Shao, Committee Member

Dr. Ezzatollah Salari, Committee Member

Dr. Cyndee Gruden, Dean
College of Graduate Studies

The University of Toledo

July 2019

Copyright 2019, Abhishek Mukherjee

This document is copyrighted material. Under copyright law, no parts of this document may be reproduced without the expressed permission of the author.

An Abstract of
Recovering skin conductance responses in under-sampled
electrodermal activity data from wearables

by

Abhishek Mukherjee

Submitted to the Graduate Faculty as partial fulfillment of the requirements for the
Masters of Science Degree in Computer Science

The University of Toledo
July 2019

One of the main benefits of wearables is their ability to collect physiological data in a minimally invasive manner. Limitations in the wearable form factor and the desire for long battery life have necessitated the use of low sampling frequencies in such devices. We consider the recovery of skin conductance responses (SCRs) from under-sampled electrodermal activity(EDA) data, where the sampling frequency is so low that standard SCR analysis methods for EDA such as peak detection fail altogether. We fit a parametric regression model with a Bateman bi-exponential functional form to under-sampled EDA data in a sequential manner in order to recover the shapes and peak locations of SCRs, which may be overlapped. We employ prior distributions on parameters based on physiological constraints and findings from previous studies on EDA in our estimation procedure. We demonstrate that our proposed methods are able to accurately recover SCR features with higher accuracy than spline-based interpolation methods on both a simulated and a real data set

Acknowledgments

Firstly, I would like to express my utmost gratitude to my advisor, Dr. Kevin S. Xu, for his patience, motivation, and knowledge. He was a constant source of motivation and guidance. I am also grateful to the other two members of my committee, Dr. Qin Shao and Dr. Ezatollah Salari, for their support and their helping me in overcoming numerous obstacles that I have been facing in my Master's thesis. I thank my fellow lab-mates in IDEAS lab Rehan, Ruthwik, Eddie, Brian, Maysam, and Makan for the stimulating discussions, for the sleepless nights we were working together before deadlines. I would also like to say a word of thanks to the two labeling experts, Eddie and Maysam, who were involved in labeling the data. Without their passionate participation and input, the thesis could not have been successfully conducted. Last but not the least, I would like to thank my parents: my mom, Munmun Mukherjee, and my dad, Ashok Kumar Mukherjee, for supporting me throughout my Master's duration and in writing this thesis as well as my life in general.

Contents

| | |
|---|-------------|
| Abstract | iii |
| Acknowledgments | iv |
| Contents | v |
| List of Tables | viii |
| List of Figures | ix |
| List of Abbreviations | xi |
| List of Symbols | xii |
| 1 Introduction | 1 |
| 1.1 Scope of the contribution | 5 |
| 2 Background and Related Work | 6 |
| 2.1 Electrodermal Activity | 6 |
| 2.1.1 Other Related Work | 10 |
| 3 Observation Model | 14 |
| 3.1 Continuous-Time Model | 14 |
| 3.2 Sampled Observation Model | 15 |
| 4 Estimation Procedure | 20 |

| | | |
|----------|--|-----------|
| 4.1 | Estimation Procedure | 20 |
| 4.1.1 | Window Detection | 21 |
| 4.1.2 | Parametric Regression Model | 22 |
| 4.1.3 | SCR Parameter Estimation | 23 |
| 4.1.3.1 | Constrained Maximum-Likelihood Estimation | 23 |
| 4.1.3.2 | Maximum A Posteriori (MAP) Estimation | 25 |
| 4.1.3.3 | Dealing with Local Optima | 26 |
| 4.1.4 | Skin Conductance Recovery | 27 |
| 5 | Experiments | 28 |
| 5.1 | Experiments | 28 |
| 5.1.1 | Experiment Set-Up | 28 |
| 5.1.1.1 | Sub-sampling Procedure | 28 |
| 5.1.1.2 | Evaluation Metrics | 30 |
| 5.1.1.3 | Comparison Method: Piecewise Cubic Hermite Inter- polating Polynomials | 32 |
| 5.1.2 | Simulated Data | 33 |
| 5.1.3 | Real Data | 33 |
| 5.1.3.1 | Annotation of SCRs | 34 |
| 6 | Results | 35 |
| 6.1 | Simulated Data Experiment | 35 |
| 6.2 | Real Data Experiment | 37 |
| 6.2.1 | Effects of Sampling Rate | 42 |
| 7 | Conclusion | 43 |
| 7.1 | Conclusion | 43 |

List of Tables

| | | |
|-----|--|----|
| 6.1 | Oracle mean-absolute error metrics (\pm standard error) for SCR features over $N = 2,530$ SCRs in simulation experiment. Best metric within 1 standard error shown in bold. | 37 |
| 6.2 | Precision- and recall-based mean-absolute error metrics (\pm standard error) for SCR features in simulation experiment. $N = 2,420$ SCRs for precision-based metrics for all methods, and $N = 2,530$ SCRs for recall-based metrics for all methods. Best metric within 1 standard error in each category shown in bold. | 37 |
| 6.3 | Oracle mean-absolute error metrics (\pm standard error) for SCR features over $N = 790$ SCRs in real data experiment. Best metric within 1 standard error shown in bold. | 39 |
| 6.4 | Precision- and recall-based mean-absolute error metrics (\pm standard error) for SCR features in real data experiment. $N = 537$ SCRs for precision-based metrics for MLE and MAP, $N = 542$ SCRs for precision-based metrics for PCHIP, and $N = 790$ SCRs for recall-based metrics for all methods. Best metric within 1 standard error in each category shown in bold. | 42 |

List of Figures

| | | |
|-----|--|----|
| 1-1 | EDA signal decomposed into SCRs and baseline | 2 |
| 1-2 | EDA signal with various sampling rates | 3 |
| 2-1 | Figure illustrating the various SCR features. | 8 |
| 3-1 | Continuous-time model for an SCR $\mu_i(\theta_i; t)$ and its sampled version μ_i with the 4 SCR parameters | 16 |
| 5-1 | Comparison of the under-sampled trace for 4 different initial phase shifts/jitters | 29 |
| 5-2 | An illustration of Precision based MAE | 31 |
| 5-3 | An illustration of Recall based MAE | 32 |
| 6-1 | Scatter plots of observed (actual) and recovered SCR features by various methods in simulated data experiment | 36 |
| 6-2 | Comparison of skin conductance recovery methods on real data | 38 |
| 6-3 | Scatter plots of observed (actual) and recovered SCR features by various methods | 40 |
| 6-4 | Recall-based error metrics for various methods as sample period is varied | 41 |
| A-1 | Comparison of the various methods of reconstructions for user1. | 51 |
| A-2 | Comparison of the various methods of reconstruction for user2. | 51 |
| A-3 | Comparison of the various methods of reconstruction for user3. | 52 |
| A-4 | Comparison of the various methods of reconstruction for user4. | 52 |
| A-5 | Comparison of the various methods of reconstruction for user6. | 53 |

| | | | |
|-----|--|-----------|----|
| A-6 | Comparison of the various methods of reconstruction for user7. | | 53 |
| A-7 | Comparison of the various methods of reconstruction for user9. | | 54 |

List of Abbreviations

| | |
|-------------|---|
| EDA | Electrodermal Activity |
| SCL | Skin Conductance Level |
| SCR | Skin Conductance Response |
| aSCR | anticipatory SCR |
| ISI | Inter Stimulus Interval |
| ANS | Autonomic Nervous System |
| EEG | Electroencephalogram |
| eSCR | evoked SCR |
| MSE | Mean Square Error |
| LTI | Linear Time Invariant |
| PPG | Photoplethysmograph |
| PRV | Pulse Rate Variability |
| ECG | Electrocardiogram |
| SSE | Sum of Squared Errors |
| MLE | Maximam Likelihood Estimate |
| MAP | Maximum A Posteriori |
| FFT | Fast Fourier Transform |
| MAE | Mean Absolute Error |
| PCHIP | Piecewise Cubic Hermite Interpolating Polynomials |

List of Symbols

| | |
|------------------|--|
| τ_1 | the time constant for decay portion of the SCR. |
| τ_2 | the time constant for the rise portion of the SCR. |
| α_i | amplitude of the <i>ith</i> SCR |
| δ_i | the time difference between the actual onset time and the last sample prior to the onset |
| μ | Representation of the continuous time Bateman function |
| θ_i | The vector representation of the Bateman parameters |
| W | Window Length |
| T | Sampling duration |
| f_d | Sampling rate of the original EDA trace |
| f_s | Under-sampled trace frequency |

Chapter 1

Introduction

Wearable computers, including fitness bands and smart watches, offer tremendous potential to continuously collect a person’s physiological data in a “free-living” setting and in a minimally invasive manner. Biometric sensors and portable devices are being increasingly embedded into our everyday life, creating the need for robust physiological models that efficiently represent, analyze, and interpret the acquired signals. They typically rely on small sensors for capturing data, portable devices for temporal storage, and the use of wireless networks for (periodic) data transfer to a database. The large volume of recordings from these sensors, their use in every-day life and beyond specialized places like clinics, the potential variability in the data quality, and the limited resources of appropriately trained people for the corresponding signal analysis underscore the need of automatic ways to process them. One such physiological signal is electrodermal activity (EDA), which is readily measured by a wearable wristband and reflects the emotional and sympathetic responses of a person [6]. Electrodermal activity (EDA) is one of the most widely used psychophysiological signals. It is related to the sympathetic nerve activity through the changes in the levels of sweat in the ducts that result in the observed skin conductance response (SCR) fluctuations. EDA has been used in many applications including stress detection [16], content valence classification [30], and classifying autonomic nervous system

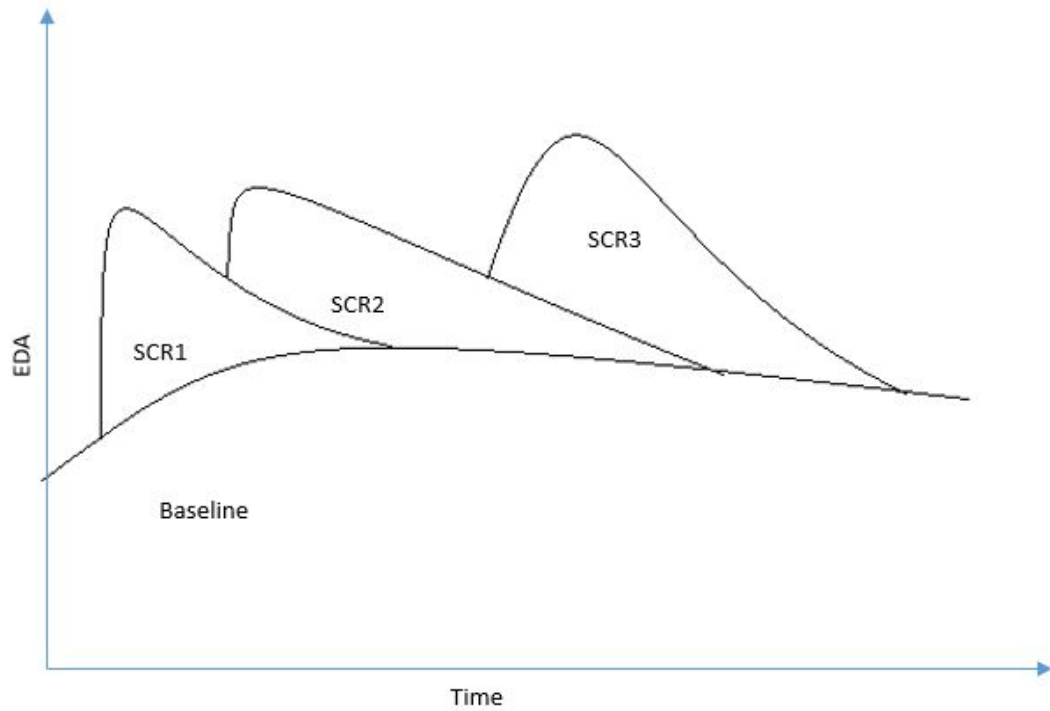


Figure 1-1: Example of an EDA signal decomposed into individual SCRs and baseline component.

activity [27].

EDA is commonly measured by the skin conductance, which consists of two main components: a slowly-varying tonic component, often referred to as the baseline or skin conductance level (SCL), and a phasic component consisting of short-lived skin conductance responses (SCRs). An SCR is a discrete event of sweat expulsion that temporarily increases the skin conductance, peaking about 1 to 3 seconds after the SCR onset. The skin conductance then gradually decreases as the sweat diffuses. SCRs are often overlapped in time, with the sweat expulsion of one SCR occurring while the sweat from a previous SCR is diffusing, as shown in Fig. 1-1.

In a lab-based setting, EDA has typically been collected at sample rates in the range of 200 Hz to 400 Hz, although it is often low-pass filtered with a cut-off frequency in the range of 20 Hz to 35 Hz prior to analysis [34, 7]. Recently the focus has shifted

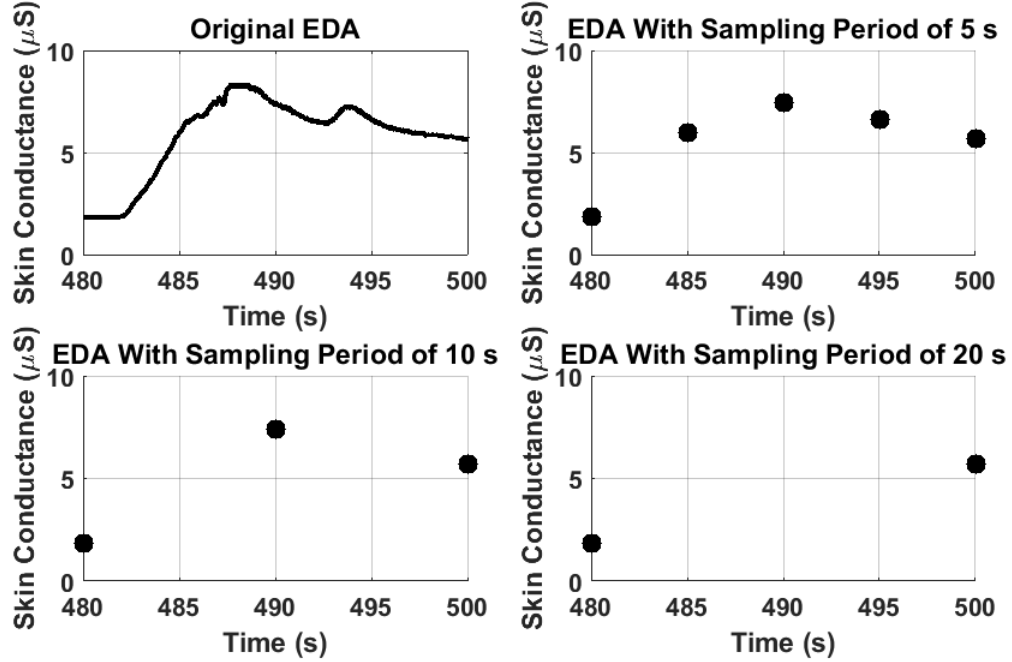


Figure 1-2: EDA signal with various sampling rates. Note the loss of the second smaller SCR at 495 s at a sampling period of 5 s and the loss of the functional form at a sampling period of 20s.

to collecting EDA signals out-side the laboratory in the wild with wearable devices that can measure continuously, privately logging and/or wirelessly streaming data. Commercial wearables typically use much lower sampling frequencies necessitated by the form factor and the desire for long battery life. For example, the clinical-grade Empatica E3 and E4 wristbands sample EDA at 4 Hz [14], and the consumer-grade Microsoft Band 2 samples EDA at 0.2 Hz [25].

The latter is particularly problematic for analyzing SCRs because a sampling rate of 0.2 Hz results in 1 sample taken every 5 seconds, which makes it highly likely that the shape of an SCR, particularly the peak, is not preserved. We refer to this setting as the *under-sampled* setting, where the sampling frequency is not high enough to directly observe the shape of SCRs, as shown in Fig. 1-2.

Psychophysiological research has established a direct relationship between electrodermal activity (EDA) and the reaction of the body to stimulus. By detection skin

conductance responses (SCRs) it is possible for researchers to identify and quantify a subject’s reaction to a given stimulus. This makes the detection and recovery of such phenomenon useful for estimation of stress levels, level of engagement with media, analysis of mental health disorders, and other applications. Along with the detection of evoked SCRs (anticipatory SCRs or aSCRs) to serve as an indicator for successful fear conditioning or to collect responses to an evoked aversive event [6], much focus has recently been on the successful detection of SCRs in a “natural and free” setting as opposed to a tightly controlled experimental environment. While recent advances in wearable technology, espoused in such as the Affectiva Q sensor and the Empatica E4 sensor [14], has made ambulatory, unobtrusive, and continuous measurement of EDA possible, the limitations of current battery technology limits their efficiency when monitoring individuals for longer durations. This is due to the high sampling rate (e.g, E4 sensor samples EDA at 4 Hz) of such sensors which significantly impact the power budget of these devices.

Recently, [18] used a context aware mobile computing that used wearable sensors to acquire information about the user and the performed activity. It says that continuous sensing rapidly depletes the wearable systems energy which is said to be a constrained source. To reduce the energy consumption it reduces the number of required sampled observations. Thus, this strategy of selective sampling is a method of deviates from the norm of continuous monitoring to selected time points, while keeping the accuracy of tracking the users current activity as high as possible.

In an uncontrolled environment, the temporal gap between two stimuli can be short enough to make the recovery of of one response overlap with the following SCR. The short inter-stimulus interval (ISI) presents itself as one of the main limitations in detection of SCRs “in the wild” [6, 11]. While in the past several efforts have been undertaken to detect SCRs with short ISIs, these studies have been limited to data sampled at a high rates. This restricts the use of such techniques to wearables that

can maintain such a high sampling rate, which constrains the battery life of such technology.

Although wearables such as the Microsoft Band2, which logs data once every 5 seconds, have proven to be an asset when monitoring individuals over longer period of time, such a low sampling rate exacerbates the problem of detecting SCRs under short ISI regimes. Fig. 1-2 shows the detrimental effect of down-sampling an EDA signal with short ISI. In the traditional setting with sufficiently high sampling rate, analysis of SCRs typically involves identifying the SCRs and then computing a set of features describing the SCR shape, such as its amplitude and rise time. Even though the 4 Hz sampling rate of the Empatica wristbands is lower than ideal, it is sufficiently high that it still allows SCR shapes to be observed and their features to be computed with high accuracy.

1.1 Scope of the contribution

In this thesis, the challenge of recovering SCRs from under-sampled skin conductance data has been addressed by proposing a parametric regression model for SCR shapes. Further a maximum-likelihood and maximum a posteriori probability estimators for the parameters which incorporate physiological constraints were also evaluated. Using the parameter estimates, the SCR shapes were recovered in a sequential manner that allows in separation of overlapping SCRs, enabling SCR analysis by computing features for each SCR.

Further the proposed estimation approach has been compared with a spline-based interpolation method on both a simulated and a real data set and find that our approach recovers SCR shapes with higher accuracy. The contribution suggests that using wearables with low sampling rates may be viable for collecting EDA data in cost-constrained or battery life-constrained settings while still enabling SCR analysis.

Chapter 2

Background and Related Work

2.1 Electrodermal Activity

The concordance of skin conductance Level (SCL) with the autonomic nervous system (ANS) is manifested in the activity of the eccrine sweat glands. These glands cause a sweat expulsion that is responsible for observed SCRs. This variation in the level of skin conductance (SC) is what is predominantly referred to as EDA [6]. Along with thermo-regulation, SCL has been found to be complementary to reflections of cerebral cortical activity as measured by electroencephalographic testing (EEG) [21] and possesses a positive correlation with physiological arousal [29]. This is particularly seen during emotional changes which makes EDA an important metric for ANS activity for the purposes of psychophysiological research.

Electrodermal activity (EDA) data has been characterized as a combination of a slowly-varying baseline component, often denoted by the skin conductance level (SCL), and a transient component consisting of short-lived skin conductance responses (SCRs). The two signal types are often referred to as the tonic and phasic components of EDA, respectively. The rapid rises typically seen in EDA signals are attributed to the phasic activity whereas asymptotic decay is attributed to the slowly drifting tonic signal [6, 11]. Due to the association of variation in the skin conductance and

psychological state, EDAs have proven to be an alternative window to record users' psychology and have led to considerable work ranging from stress detection[23] to content and audience segmentation [20]. Since the rapid change in skin conductance via sweat expulsion is triggered by sudomotor neuron firing [4], most of the applications using EDA signal to infer psychological state rely on detecting the SCRs embedded in the EDA.

A heuristic approach for the study of EDA was demonstrated decades ago when Féré measured skin resistance [11] by passing current between two electrodes placed on the skin. He found that there is a sudden, momentary drop in the skin resistance in response to different stimuli. This method for measuring skin conductance has been termed the exosomatic method. In contrast, the endosomatic method does not require the passage of an electric current through the skin, but the endosomatic method, uses a subject and galvanometer circuit to measure changes in resting electromotive force, or voltage of the skin. [13],[6]. With the necessity for measuring affective, autonomic stress for prolonged periods of time, a longer battery life that supplies a stable continuous current for high accuracy measurements is a necessity for wearables.

SCRs are characterized by a rapid increase in skin conductance, reaching a peak about 1 to 3 seconds after the SCR onset, followed by a slow exponential decay. Different SCRs will have different shapes that are often characterized by a set of quantitative features as illustrated in Fig. 2-1.

Some commonly used features [6] include

- Amplitude: the difference between the skin conductance values at the SCR peak and onset times.
- Rise time: the time elapsed from the SCR onset time to the SCR peak time.
- Half-recovery time: the time elapsed from the SCR peak time to the time at which the SCR decays to half of the SCR amplitude.

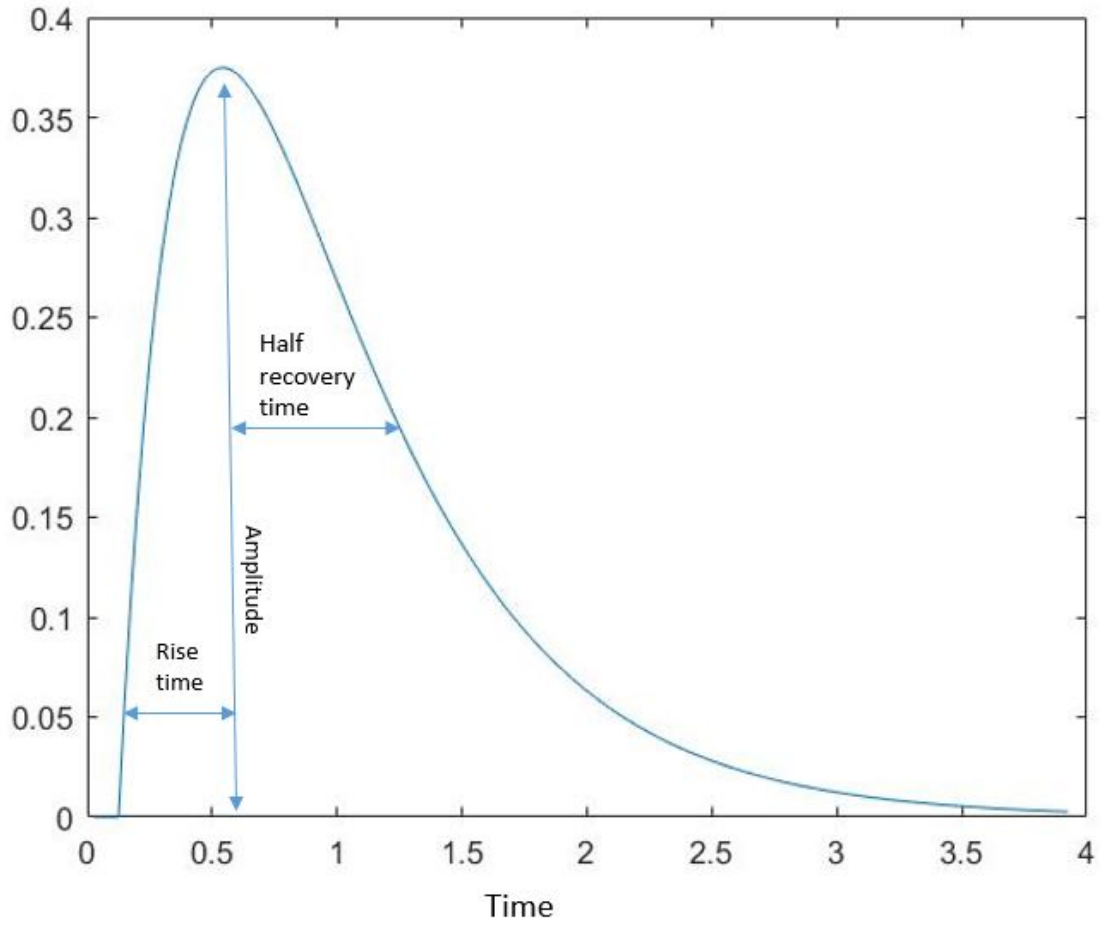


Figure 2-1: Figure illustrating the various SCR features.

SCR analysis involves extracting the SCRs from the observed EDA signal and then computing these features on the extracted SCRs.

Due to the significant time commitment involved in manually extracting SCRs, there has been significant interest in automatically detecting SCRs in EDA in order to automatically compute the SCR features. Most early algorithms to detect SCRs relied on the detection of peaks and troughs in the EDA data. For example, Storm et al. [32] developed a computer program that could automatically extract SCRs by detecting peaks and troughs in the EDA signal and classify these as SCRs. This method also provided mean estimates for the baseline and amplitude of the detected SCRs. Since the method used time derivatives to detect peaks and valleys in the data,

contiguous SCRs result in an inflection point in the data without a detectable peak. This results in incorrect scoring of two events as a single event. It could also provide a mean estimate for the baseline and the amplitude of the SCRs. Peak detection has many limitations but is still viewed as the “gold standard” for SCR detection.

An alternative approach to peak detection involves building a mathematical model for the different EDA components and how they combine to form the observed EDA signal. It is typically assumed that the EDA signal $y(t)$ is generated as the output of a linear time-invariant system where the input signal $x(t)$ is the SCR events signal or phasic driver controlling the SCR onset times. The SCRs are modeled by a convolution of the phasic driver $x(t)$ with a filter with impulse response $h(t)$ that matches the shape of a typical SCR. The output of this convolution is then added to the baseline term $b(t)$ and observation noise $n(t)$, resulting in the observation model

$$y(t) = h(t) * x(t) + b(t) + n(t). \quad (2.1)$$

The typical choice of impulse response is a bi-exponential form commonly referred to as the Bateman function [4, 15, 17]

$$h(t) = e^{-t/\tau_1} - e^{-t/\tau_2}, \quad t \geq 0 \quad (2.2)$$

where $\tau_1 > \tau_2 > 0$ are the time constants for the decay and rise portion of the SCR, respectively. The time constants are often assumed to differ across different test subjects.

From this mathematical model, SCRs can be recovered by inverting the model using deconvolution methods Alexander et al. [1] and variants including non-negative deconvolution [4] and sparsity-constrained deconvolution [15, 17]. Another approach to exploit the sparse nature of the phasic driver $x(t)$ involves decomposing the signal into atoms derived from a knowledge-driven dictionary [9, 30]. The EDA-specific

dictionary contains both tonic and phasic atoms, such as Bateman functions with different (τ_1, τ_2) parameters, to model both components of EDA. A third approach involves estimating the impulse response function from data rather than using a parametric form like the Bateman function [3].

2.1.1 Other Related Work

A deconvolution-based method was proposed by [1] whereby SC data was deconvolved with a bi-exponential function. This process would then reveal a driver function which consisted of a sequence of discrete bursts with short time constants. Peak detection then was performed with this driver function in order to extract peaks. These peaks were then re-convolved with bi-exponential functions in order to reconstruct the original signal. For cases where the shape of the impulse response did not conform to the frequently employed bi-exponential function, an iterative procedure was applied to an initial estimate of the peaks location. The peaks were then updated iteratively until no further changes occurred in the location of the detected peaks. Although this method successfully scaled to different data sets, the method was not sufficiently autonomous for wearables use as it required continuous monitoring of peak locations and, as typical for curve-fitting methods, is dependent upon initial estimates of the peak locations.

SCRs were grouped into anticipatory, evoked, and spontaneous SCRs by [2] and parameterized them with different neural input functions. These function groupings represent a priori knowledge of the time windows of their occurrence as well as their expected shapes. The three neural input functions were assumed to be Gaussian bumps parameterized by amplitude, timing and duration. For aSCRs, amplitude, timing, and duration were estimated with a trial-wise method within an anticipation window. Although the amplitude for evoked SCRs (eSCRs) were estimated in a similar manner the aSCRs, the timing and the duration are assumed to be constant

across all the data sets.

Another iterative curve-fitting procedure developed to tackle overlapping SCRs with short ISIs was described by [22]. Here, individual SCRs were fitted with an asymmetric sigmoid and as well as an exponential function. The model parameters were then iteratively updated in order to minimize mean squared error (MSE). The iterative optimization procedure continued until the fitted residuals between model parameters (latency, rise-time, decay of the SCR) and the data was less than 5%.

A recent approach by [4] for decomposition of overlapping SCRs was by incorporating the “poral valve model” [12]. The fundamental hypothesis behind this model was that it considers the SCR shape to be attributed to a physiological processes of unconditional diffusion and pore opening. The unconditional diffusion process was ascribed to flatter SCRs and the pore opening process to SCRs with steeper rises. Since the standard deconvolution method as described by [1] with bi-exponential functions yielded peaks which crossed the baseline which violates the assumption of non-negative peaks, [4] used a non-negative deconvolution procedure. The values of the two time constants in the bi-exponential function were also varied so that the various shapes of the SCR could be taken into account.

Since a convex objective function ensures optimal solutions for the large number of available local search algorithms, recent efforts were made to cast the decomposition of EDA as a convex optimization problem in order to take advantage of this property. [15] estimated the tonic and the phasic signal of EDA by minimizing a quadratic cost function. The tonic signal was represented as a sum of cubic B-spline functions and the phasic part by the bi-exponential function. The sudomotor nerve bursts representing the phasic component was modeled using a Poisson distribution.

Sparse nature of sudomotor bursts was exploited by [9, 30] to propose a greedy sparse representation to decompose the signal into atoms derived from a knowledge driven dictionary. The EDA specific dictionary contained both tonic and phasic

atoms to model the slow varying tonic part and the rapid phasic response of EDAs. Although the algorithm had an advantage of not using a pre-determined structure to fit the model, the use of an over-complete dictionary leads to a non-convex problem which doesn't ensure that a globally optimal solution can be reached.

Most of the aforementioned methods for SCR analysis were designed for high-quality EDA data collected in a traditional lab-based setting. EDA collected from wearables presents additional challenges, such as under-sampling and the presence of motion artifacts. [17] recently proposed a compressed sensing method to recover SCRs from EDA data. Motivated by the potential use in wearables, they proposed a method to account for sudden changes in the baseline due to rapid changes in the positions of the sensors from motion. An alternative to directly accounting for motion artifacts into the EDA model is to first detect and remove portions of data with motion artifacts, which is often accomplished using classification or anomaly detection algorithms [33, 35]. Contrary to previous methods, [17] incorporated the non-ideality of the environment that a wearable is operating in. This can cause the baseline to have a larger magnitude than other noise signals, and as such cannot be assumed to be a noised signal as assumed in the standard deconvolution settings. This new methodology discretized the EDA signal into T time steps and then used the structure of the baseline to linearly transform the discretized signal so that the transformed baseline and the SCR bursts could be jointly recovered. Although this method worked well in the controlled environment setting when predicting evoked SCRs within an anticipated time window, the model begins to sacrifice significant accuracy as the discretization size T becomes larger thereby limiting its use in low sample rate devices.

Although we are not aware of prior work investigating the effects of EDA sampling rate (particularly under-sampling) in wearables, the effects of sampling rates for other types of sensors in wearables have been studied. [19] investigated the effects of accel-

erometer sampling rates on activity recognition accuracy and battery life. A recent study by [10] to assess the influence of sampling frequency on Pulse Rate Variability (PRV) shows that 25 Hz can be a potentially reliable sampling frequency for PRV measurements derived from photoplethysmography (PPG) data. Generally, for clinical research electroencephalogram (EEG) is commonly sampled at around the sampling rates of 250-500 Hz but for wearables EEG sampling rates can vary based on the system. For example, [28] developed an algorithm to use 150 Hz as the sampling rate in their wearable system. Recently,[31] extracted the heart rate variability from Electrocardiogram (ECG) wearables with a precision of 1ms at an approximate sampling frequency of 120Hz. Empatica’s E4 samples the PPG signal to derive Heart rate and Inter-Beat-Intervals at an acquisition rate of 64 samples/sec.

Despite this previous work in identifying SCRs, significant contributions can still be made by the development of a methodology for a flexible, low-sample rate method suitable to a wearable environment. This means developing a method that operates in both a noisy, non-controlled environment with a low-sample rate signal.

Chapter 3

Observation Model

3.1 Continuous-Time Model

As previously mentioned the continuous time EDA signal $y(t)$ can be decomposed into a slowly varying baseline signal $b(t)$, often referred to as the tonic component of EDA or the skin conductance level (SCL), and a phasic component consisting of a series of short-lived skin conductance responses (SCRs). We assume the SCRs follow the Bateman function form (2.2), but unlike the prior work discussed in Section 2.1, we assume that different SCRs (within the same test subject) can have different time constants, as prior work has found that there can be significant intra-subject variation in SCR shapes. As a result, the system is no longer time-invariant. Each SCR event or phasic driver is modeled by a scaled and shifted impulse function

$$x_i(t) = \alpha_i \delta(t - t_i), \quad (3.1)$$

where t_i denotes the onset time of the i th SCR, α_i scales the amplitude of the SCR, and $\delta(\cdot)$ denotes the Dirac delta function, an impulse with unit amplitude. We denote the Bateman function for the i th SCR by

$$h_i(t) = e^{-t/\tau_{1i}} - e^{-t/\tau_{2i}}, \quad t \geq 0, \quad (3.2)$$

where $\tau_{1i} > \tau_{2i} > 0$. The SCR signal containing the sum of all SCRs then has the form

$$u(t) = \sum_{i=1}^N \alpha_i h_i(t), \quad (3.3)$$

where N denotes the number of SCRs. The SCR signal $u(t)$ is assumed to be superimposed on the baseline signal $b(t)$ and observation noise $n(t)$ so that the continuous-time EDA signal can be represented as

$$y(t) = u(t) + b(t) + n(t) = \sum_{i=1}^N \alpha_i h_i(t) + b(t) + n(t). \quad (3.4)$$

The “short lived” bursts which manifest as sudden changes in skin conductance can be rightly understood, physiologically, as episodes of sweat expulsion due to psychological arousal occurring in response to stimuli. The SCR events form a sparse selection from the subset of instances when the user has responded with a physiological change to a psychological arousal. The steep rise of the bi-exponential function represents the rapid change in the skin conductance due to sweat expulsion and the subsequent pooling of sweat while the slow decay can be interpreted as the steady but slower evaporation of sweat from the skin. Furthermore, the slowly drifting tonic component (baseline, $b(t)$) represents the alteration in conductance due to the process of absorption of sweat into surface of the skin. Since the baseline is dependent on temperature, humidity and other environmental factors along with psychological arousal, it can be considered as an unwanted component of the EDA signal.

3.2 Sampled Observation Model

The continuous-time EDA signal $y(t)$ is never observed when using digital systems to acquire EDA; rather, a sampled version \mathbf{y} is observed. Our objective is to recover the continuous-time EDA $y(t)$ from the samples \mathbf{y} as accurately as possible.

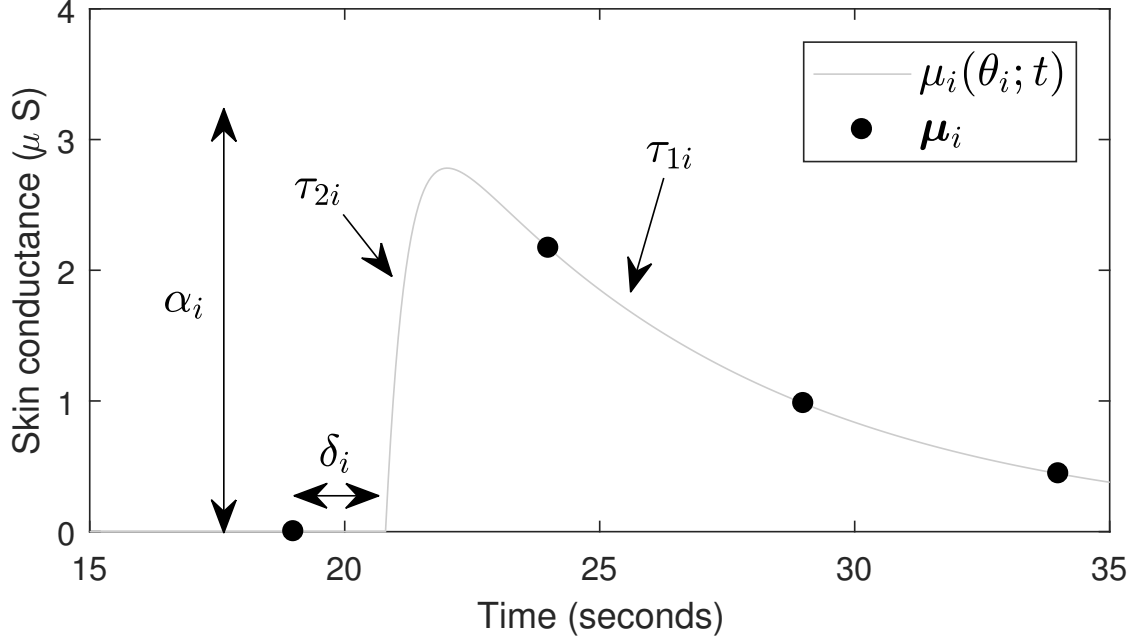


Figure 3-1: A realization of the continuous-time model for an SCR $\mu_i(\theta_i; t)$ and its sampled version μ_i with the 4 SCR parameters illustrated. α_i scales the amplitude of the SCR. δ_i controls the exact onset time of the SCR. τ_{1i} and τ_{2i} are time constants for the decay and rise, respectively, of the SCR and also affect the amplitude.

We denote the sampling frequency by f_s and the sampling period by $T = 1/f_s$. Prior work has assumed that the sampling frequency is high enough so that one can assume that the sampled EDA vector \mathbf{y} captures all of the useful information from the continuous-time EDA signal $y(t)$. For example, with a sampling frequency of 20 Hz, one can visually identify the peak time of an SCR to within $1/20 = 0.05$ seconds, which is often sufficient for practical purposes. However, with a sampling frequency of 0.2 Hz, one can only visually identify the peak time of an SCR to within $1/0.2 = 5$ seconds, which is highly problematic considering that an SCR typically peaks about 1-3 seconds after its onset [8].

To address this lack of time resolution in the under-sampled regime, we propose to estimate the continuous-time EDA signal by first estimating each SCR. The contribution of an individual SCR i to the observed signal $y(t)$ is given by $\alpha_i h_i(t)$. Let s_i denote the time of the last sample prior to the onset time t_i . Let $\delta_i = t_i - s_i$ denote

the time difference between the actual onset time t_i and the last sample prior to the onset. Let $\theta_i = \{\alpha_i, \delta_i, \tau_{1i}, \tau_{2i}\}$, where τ_{1i} and τ_{2i} denote the Bateman parameters governing the decay and rise of SCR i , respectively. Then, the contribution of SCR i can be written as

$$\mu_i(\theta_i; t) = \alpha_i \left[\exp\left(-\frac{t - s_i - \delta_i}{\tau_{1i}}\right) - \exp\left(-\frac{t - s_i - \delta_i}{\tau_{2i}}\right) \right], \quad t \geq s_i + \delta_i \quad (3.5)$$

Consider a window of W samples beginning at s_i . The sampled version of SCR i would be a vector $\boldsymbol{\mu}_i$ of length W where the j th sample takes on the value

$$\begin{aligned} (\boldsymbol{\mu}_i)_j &= \mu_i(\theta_i; s_i + jT) \\ &= \alpha_i \left[\exp\left(-\frac{jT - \delta_i}{\tau_{1i}}\right) - \exp\left(-\frac{jT - \delta_i}{\tau_{2i}}\right) \right], \quad j \in \{0, 1, \dots, W\}. \end{aligned} \quad (3.6)$$

An illustration of one realization of an SCR generated using the function $\mu_i(\theta_i; t)$ and its sampled version $\boldsymbol{\mu}_i$ are shown in Fig. 3-1 along with the roles of the 4 SCR parameters.

From (3.6) and the continuous-time observation model (3.4), the sampled version of the continuous-time EDA signal $y(t)$ can be approximated by

$$\mathbf{y} = \sum_{i=1}^N \boldsymbol{\mu}_i + \mathbf{b} + \mathbf{n}, \quad (3.7)$$

where \mathbf{b} and \mathbf{n} are sampled versions of $b(t)$ and $n(t)$, respectively, with samples taken every T seconds. The approximation becomes exact in the limit where the window length $W \rightarrow \infty$ so that the full contribution of each SCR is captured in (3.7).

Motivated by efficacy of under-sampling for the increased usefulness of wearables, a modeling for this sampling scheme was developed. This scheme can be considered the basis to detect SCRs in a severely under-sampled setting. We begin by sampling the EDA data uniformly once every T seconds followed by peak detection on the

samples. The primary assumption of this procedure is that the under-sampled signal will be very smooth as a byproduct of such a low sampling rate and that no false peaks will be detected because of noise. That is, every detected peak in this process will be mapped to a peak in the high sample rate or true signal.

Although the peaks in the under-sampled signal can be considered to be true peaks in the sense that they correspond to peaks in the true signals, the locations of such peaks will be well off due to the limited time resolution intrinsic to such a low sample rate. In addition to this, the associated functional form of the time series will be lost as the signal is down-sampled.

To retrieve the correct location of the onsets and the peaks as well as the other parameters time windows are formed around the peak and the data is then fit into a bi-exponential functional form consistent with skin conductance changes. Due to the severe under-sampling, it is assumed that the peak in the under-sampled signal has been shifted from the true location and is closer to the onset rather than the peak in the original signal. Given the fact that the rise time of the original signal is between 1-3 secs[6] and with a time shift of δ seconds we can assume that there will be a sample between the onset and the peak which will have a high amplitude then the next sample which is again T seconds away. Since T is very high the amplitude of the next sample will lie in the decaying tail of the SCR making it lower in amplitude. Hence, it can turn out to be a good assumption that the peak in the under-sampled signal is closer to the onset than the peak in the original signal. Therefore, the time windows of samples start at the detected peaks to the next W samples. The onset of the SCR can lie anywhere between two consecutive samples, and the time difference between the sampling and the onset instant is represented as δ hence we form time windows of samples starting from the detected peaks to the next W samples. The onset of the SCR can lie anywhere between two consecutive samples, this time difference between the sampling and the onset instant is assigned to the Greek alphabet δ . Since the

data is sampled every T seconds, δ is constrained to be between 0 to T seconds.

Chapter 4

Estimation Procedure

4.1 Estimation Procedure

Given the parametric form (3.5) we assume for an SCR, it would be possible to reconstruct the SCR by estimating the values of the parameters $\theta_i = \{\alpha_i, \delta_i, \tau_{1i}, \tau_{2i}\}$ from the sampled version $\boldsymbol{\mu}_i$. However, we do not observe $\boldsymbol{\mu}_i$; rather, we observe only the sampled EDA signal \boldsymbol{y} , which is a sum of all N SCRs along with the baseline signal and observation noise, as given in (3.7). Multiple SCRs may overlap in time, so we propose to estimate SCRs sequentially, beginning at the end of the signal, i.e. with SCR N . We then subtract our estimate of SCR N from \boldsymbol{y} in order to estimate SCR $N - 1$, and so on. The end result is analogous to performing deconvolution in a sequential manner by estimating a single SCR at a time.

The estimation procedure is summarized by the following steps:

1. Detect windows around SCRs using peak detection (Section 4.1.1).
2. Set current window to the last window (in time) N (the number of detected SCRs).
3. Estimate SCR parameters for current window (Section 4.1.3).
4. Subtract contribution of current SCR from sampled EDA signal \boldsymbol{y} (Section

4.1.4).

5. If current window is the first window (in time), then terminate. Otherwise, move current window back by 1 and return to step 3.

4.1.1 Window Detection

In order to reconstruct an SCR from the sampled EDA \mathbf{y} , we must first detect a window of W samples containing the SCR to use for estimating the SCR parameters θ_i . Since an SCR peaks several seconds after its onset, we propose to use peak detection to detect the window. Due to variations in the phase of the samples, a peak detected from the sampled EDA \mathbf{y} may occur slightly before or after the actual peak time of the SCR that would be observed in the continuous-time signal $y(t)$. Thus, in order to ensure that the window contains the onset of the SCR, we start the window Q samples prior to the detected peak. For SCR i , we denote this start time by \hat{s}_i , as it is an estimate of s_i , the actual time of the last sample prior to the SCR onset time t_i . An SCR generally peaks 1-3 seconds after onset, and we add a buffer of 5 seconds to account for the initial shift or phase of the samples, so we can expect an SCR onset to be within 8 seconds prior to the peak. Thus we choose $Q = \lceil 8/T \rceil$ samples, which is 2 samples for a sampling frequency of 0.2 Hz. We set the window length to $W = \lceil 30/T \rceil$ samples, noting that most SCRs have exhibited significant decay by that point. The inter-stimulus interval in lab experiments with evoked SCRs is also commonly set to 30 seconds [5].

A downside of using peak detection is that it may falsely detect or miss many SCRs. To avoid false detections, we set the minimum peak prominence (relative amplitude) to $0.05 \mu\text{S}$. Missing SCRs is a greater concern—some missed SCRs are simply not detectable at such low sampling rates. To investigate the effects of missed SCRs from peak detection, we also run experiments using oracle windows, i.e. windows

that assume oracle knowledge of the s_i 's, as we discuss later in Section 5.1.1.2.

4.1.2 Parametric Regression Model

Based on our observation model, the sampled version of SCR i is given by the vector $\boldsymbol{\mu}_i$ defined in (3.6). However, we observe only the sampled EDA \mathbf{y} , not $\boldsymbol{\mu}_i$. Our objective is to estimate $\mu_i(\theta_i; t)$ for each SCR i , which is equivalent to estimating the values of the parameters θ_i . Since SCRs may overlap in time, once we compute the estimated parameters $\hat{\theta}_i$ for SCR i , we subtract the estimated $\hat{\boldsymbol{\mu}}_i$ from \mathbf{y} to remove its contribution when estimating other SCRs. Since no SCR can come after SCR N (the last observed SCR), we compute the estimate $\hat{\boldsymbol{\mu}}_N$ directly from \mathbf{y} . We then compute

$$\tilde{\mathbf{y}}_i = \mathbf{y} - \sum_{j=i+1}^N \hat{\boldsymbol{\mu}}_j \quad (4.1)$$

which denotes the remainder of the observed EDA after subtracting out the contributions of all SCRs after i , which we use to compute the estimate $\hat{\boldsymbol{\mu}}_i$ for SCR $i = 1, \dots, N - 1$. Similarly, let

$$\tilde{y}_i(t) = y(t) - \sum_{j=i+1}^N \mu_j(\hat{\theta}_j; t) \quad (4.2)$$

denote the remainder of the continuous-time EDA signal $y(t)$ after subtracting out the contributions of all SCRs after i .

Let \mathbf{w}_i denote the window of W EDA samples constructed around SCR i , with values given by

$$\mathbf{w}_i = [\tilde{y}_i(\hat{s}_i), \tilde{y}_i(\hat{s}_i + T), \dots, \tilde{y}_i(\hat{s}_i + (W - 1)T)]^\top. \quad (4.3)$$

Our objective is to estimate the parameters θ_i for SCR i , which determine the values

of $\mu_i(\theta_i; t)$, the contribution of SCR i to the continuous-time EDA $y(t)$. We propose the following parametric regression model for SCR i :

$$\mathbf{w}_i = \boldsymbol{\mu}_i(\theta_i) + \beta_i \mathbf{1} + \boldsymbol{\epsilon}_i \quad (4.4)$$

where we have added (θ_i) to $\boldsymbol{\mu}_i$ to make explicit the dependence on the SCR parameters, β_i is a scalar intercept term, $\mathbf{1}$ denotes an all-ones column vector, and $\boldsymbol{\epsilon}_i$ denotes the vector of residuals. Notice the similarity in structure between our proposed regression model (4.4) and our sampled observation model (3.7). Our regression model (4.4) contains \mathbf{w}_i rather than \mathbf{y} to isolate the contribution of SCR i (denoted by $\boldsymbol{\mu}_i(\theta_i)$). Since the baseline tonic component $b(t)$ is known to vary extremely slowly over time, we model the baseline component over a window with a constant intercept β_i . Finally, the residual term $\boldsymbol{\epsilon}_i$ in (4.4) captures both the observation noise \mathbf{n} in (3.7) and estimation errors in SCRs $i+1, i+2, \dots, N$ that were previously estimated.

4.1.3 SCR Parameter Estimation

Given our parametric regression model (4.4), our objective is to estimate the SCR parameters $\theta_i = \{\alpha_i, \delta_i, \tau_{1i}, \tau_{2i}\}$. The parameters cannot take on arbitrary values, however, as the shape of an SCR is governed by physiological constraints. We consider two estimation approaches that account for these physiological constraints in different manners.

4.1.3.1 Constrained Maximum-Likelihood Estimation

We first consider minimizing the sum of squared errors (SSE) cost function that is used in ordinary least squares regression. The cost function is defined by

$$\text{SSE}(\theta_i, \beta_i) = \sum_{j=0}^{W-1} \left[(\mathbf{w}_i)_j - (\boldsymbol{\mu}_i(\theta_i))_j - \beta_i \right]^2 \quad (4.5)$$

and can be iteratively optimized by standard interior point methods for constrained optimization. It is known that minimizing the SSE is equivalent to maximizing the likelihood of a Gaussian distribution [26], so we refer to this estimate as a constrained maximum-likelihood estimate (MLE).

The constraints on these parameters are informed by the physiology of EDA. When sweat glands expel sweat, skin conductance is increased, so the contribution of each SCR i through $\mu_i(\theta_i; t)$ must be positive, which implies that $\alpha_i > 0$. The Bateman parameters τ_{1i} and τ_{2i} are time constants and thus both must also be positive. Since SCRs have a rapid rise and a much slower decay, the time constant responsible for the decay must be higher than the time constant associated with the rise of the SCR, which leads to the constraint $\tau_{1i} > \tau_{2i}$. Finally, the onset time shift δ_i must satisfy the constraint $0 \leq \delta_i < \delta_{\max} = QT$, where the choice of Q is discussed in Section 4.1.1. For $T = 5$ seconds, $\delta_{\max} = 10$ seconds.

The upper bounds for α_i , τ_{1i} , and τ_{2i} are set based on observations on amplitudes, rise times, and half-recovery times in prior work, including the following. Lim et al. [22] found the decay time constant τ_{1i} to be 2.98 secs and the rise time constant τ_{2i} to be 1.6 secs from 60 events. Alexander et al. [1] tested their methodology with 735 participants of various age groups, and their findings suggest that the optimal values of time constants were $(\tau_{1i}, \tau_{2i}) = (2, 0.75)$ seconds, respectively. The Handbook of Psychophysiology describes the rise time to be in between 1-3 secs and the half recovery time to be in between 2-10 secs [8]. Benedek and Kaernbach [5] found that the average maximum phasic driver amplitude α_i over a user was 6.50 with standard deviation 3.37. We choose to set upper bounds somewhat conservatively; thus, we set the upper bounds for α_i and τ_{1i} to 20 and the upper bound for τ_{2i} to 5.

4.1.3.2 Maximum A Posteriori (MAP) Estimation

The constraints described above serve to eliminate parameter values that are physiologically unlikely. An alternative approach is to utilize prior distributions for the parameters. Priors shift the probability mass of the parameter estimates towards “more frequent” values and serve as an alternative to the all-or-nothing approach of hard constraints for the upper bounds on α_i , τ_{1i} , and τ_{2i} . Since $\alpha_i > 0$, we use a Gamma distribution as the prior with shape parameter a_α and scale parameter b_α , which we denote by $\Gamma(a_\alpha, b_\alpha)$. Similarly, we use a $\Gamma(a_{\tau_1}, b_{\tau_1})$ and $\Gamma(a_{\tau_2}, b_{\tau_2})$ prior for the Bateman parameters τ_1 and τ_2 , respectively. Finally, since the onset time shift is completely random due to the time shift or phase of the samples, we place a uniform prior on δ_i with support $[0, \delta_{\max}]$.

In order to utilize the priors, we also need to assume a probability distribution for \mathbf{w}_i . The SSE is closely related to the negative log-likelihood of a Gaussian distribution [26], so we assume \mathbf{w}_i is Gaussian distributed with mean $\boldsymbol{\mu}_i(\theta_i) + \beta_i \mathbf{1}$ and covariance matrix $\sigma^2 \mathbf{I}$, where \mathbf{I} denotes the identity matrix.

Then, the log-likelihood is given by

$$\log \mathcal{L}(\theta_i) = -\frac{\text{SSE}(\theta_i, \beta_i)}{2\sigma^2} + \text{const.} \quad (4.6)$$

Combining (4.6) with the prior densities for the parameters¹, the log of the posterior probability density becomes

$$\begin{aligned} \log p(\theta_i, \beta_i | \mathbf{w}_i, \boldsymbol{\mu}_i) = & -\frac{\text{SSE}(\theta_i, \beta_i)}{2\sigma^2} + \log \Gamma(\alpha_i | a_\alpha, b_\alpha) + \log \Gamma(\tau_{1i} | a_{\tau_1}, b_{\tau_1}) \\ & + \log \Gamma(\tau_{2i} | a_{\tau_2}, b_{\tau_2}) + \frac{1}{\delta_{\max}} + \text{const.} \end{aligned} \quad (4.7)$$

¹We have implicitly assumed an improper uniform prior (i.e. no prior information) for the intercept β_i , which is easily estimated compared to the other parameters.

where

$$\log \Gamma(x|a, b) = -a \log b + (a - 1) \log x - \frac{x}{b} + \text{const.} \quad (4.8)$$

denotes the log of the probability density for a $\Gamma(a, b)$ prior. The log-posterior (4.7) can be iteratively optimized by standard quasi-Newton algorithms for unconstrained optimization to obtain the maximum a posteriori probability (MAP) estimate.

We select the hyperparameters for the Gamma priors by leveraging the findings of prior work in psychophysiology. Benedek and Kaernbach [5] report the mean and standard deviation of the estimated phasic driver amplitude α_i as well as the estimated Bateman function time constants (τ_{1i}, τ_{2i}) in their experiments. We choose our hyperparameters so that the mean and standard deviation of our priors match their reported values, resulting in a $\Gamma(3.7, 1.7)$ prior for α_i , a $\Gamma(6, 1)$ prior for τ_{1i} , and a $\Gamma(3, 0.4)$ prior for τ_{2i} . Finally, we set the variance of the residual $\sigma^2 = 0.01$.

4.1.3.3 Dealing with Local Optima

Both the SSE (4.5) and the log-posterior (4.7) are multi-modal and thus may have many local optima. In general, multiple random initializations are often employed to attempt to find the global optimum. We propose a more principled approach that exploits the nature of the local optima in our problem. Specially, the local optima are related to the choice of parametric form (3.6). For example, let θ_i^* denote the global minimum for the SSE cost function for SCR i . If we increase δ_i , then the entire SCR would be shifted to the right (later in time), which would increase the SSE, especially due to the worse estimation around the SCR peak time. We could then decrease SSE by decreasing τ_{2i} , which would improve the estimate around the peak, resulting in a local minimum.

Since the local optima are related to the relationships between δ_i and the other SCR parameters, we use multiple initializations for δ_i uniformly within its range

$[0, \delta_{\max})$. We initialize the other SCR parameters α_i , τ_{1i} , and τ_{2i} near their prior means. Finally, we initialize the intercept β_i to the minimum value in the window μ_i , since SCRs must be positive.

4.1.4 Skin Conductance Recovery

The SCR parameter estimation approaches in the previous section enable estimation of the $\mu_i(\theta_i; t)$ terms in (3.4). To complete the recovery of the continuous-time skin conductance $y(t)$, we need to estimate the sum $b(t) + n(t)$ containing the baseline signal and observation noise. We propose to do this by first subtracting the sampled versions of the estimated SCRs $\hat{\mu}_i$ from the sampled EDA \mathbf{y} . From the sampled observation model (3.7), the sum $\mathbf{b} + \mathbf{n}$ is left, i.e. the sampled version version $b(t) + n(t)$. Since the baseline signal contains the tonic component of EDA, which varies slowly over time, we use a low-pass interpolating filter based on the zero padding and the Fast Fourier Transform (FFT) [24] implemented using the MATLAB Signal Processing Toolbox `interp()` function.

Chapter 5

Experiments

5.1 Experiments

We conduct two experiments: one on a simulated data set and one on a real data set. In order to evaluate the ability of our proposed methods for recovering the continuous-time skin conductance $y(t)$, we begin with data sampled at a high rate (e.g. 20 Hz), which we treat as an accurate representation of $y(t)$. We then sub-sample the data at a much lower rate (e.g. 0.2 Hz) to obtain the under-sampled skin conductance vector \mathbf{y} , which is provided to our estimation procedure. We then compare the recovered skin conductance $\hat{y}(t)$ to $y(t)$ using several evaluation metrics that are relevant to EDA analysis.

5.1.1 Experiment Set-Up

5.1.1.1 Sub-sampling Procedure

We denote the sampling rate of the original EDA trace by f_d and the sampling rate of the under-sampled data by f_s , where $f_d \gg f_s$. To obtain the under-sampled data, the original EDA trace is sub-sampled to rate f_s by taking a sample each $T = 1/f_s$ seconds. We create 10 under-sampled data sets from each original EDA trace by varying the initial time shift or phase of the under-sampled data, which is

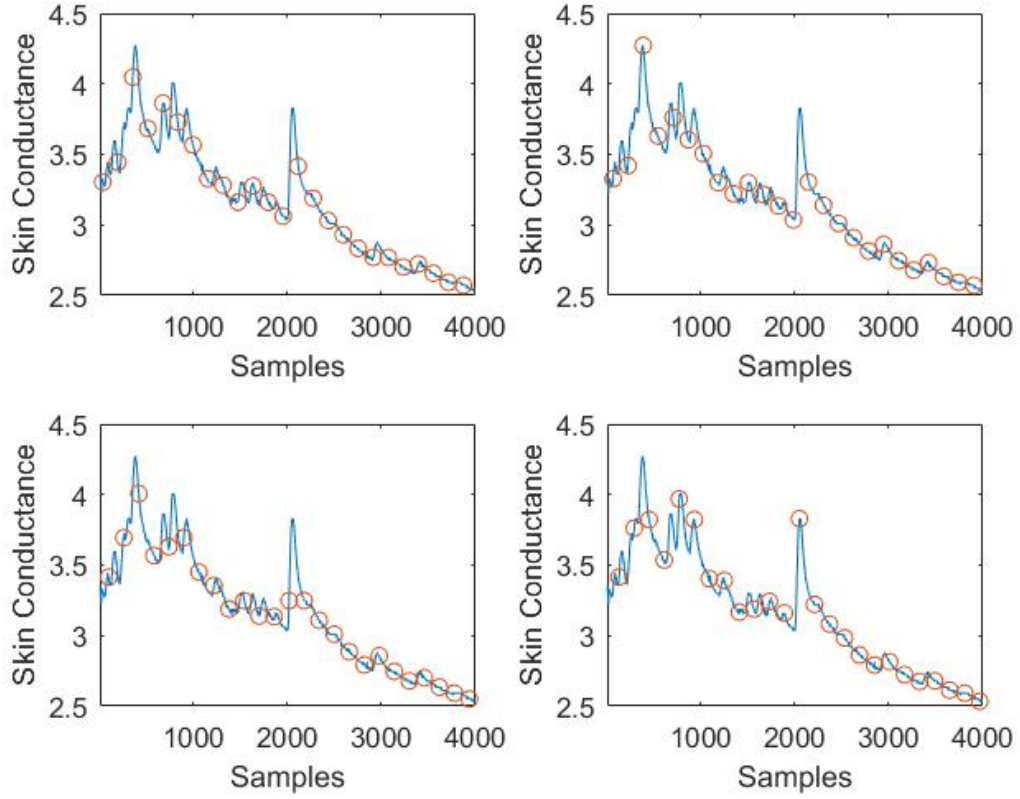


Figure 5-1: Comparison of the under-sampled trace for 4 different initial phase shifts/jitters. The figure shows that different initial shifts result in markedly different under-sampled responses.

unknown in a real under-sampled data collection setting and can take on any value in the range $[0, T)$. Figure 5-1 shows the under-sampled traces for 4 different initial phase shifts. From the plots it can be seen that different initial phase shift/jitter can result in markedly different under-sampled EDA traces. Since an SCR peaks about 1 to 3 seconds after its onset, different initial shifts can result in large differences in the appearance of the under-sampled EDA y . We uniformly space the initial shifts between 0 and $0.9T$ seconds.

5.1.1.2 Evaluation Metrics

In both experiments, we assume we have access to ground-truth labels of the onset and peak times of each SCR in the original data trace $y(t)$. Such labels are available in the simulated data experiment as part of the data creation process. In the real data experiment, the labels are created by human annotation (see Section 5.1.3.1). With ground-truth labels identified, we identify several suitable metrics to evaluate the quality of the reconstruction in a meaningful manner. Since the main drawback of under-sampling is the inability to accurately represent SCRs, we choose 4 evaluation metrics related to the appearance of SCRs in the original EDA trace: the peak time, which is the actual time at which SCR reaches its peak, and the amplitude, rise time and half-recovery time metrics described in Section 2.1.

We compute the mean absolute error (MAE) over all SCRs between each metric when computed on the original EDA trace $y(t)$ and on the reconstructed skin conductance from the undersampled EDA \mathbf{y} . In order to compute MAE, we must first match up SCRs in the reconstruction to SCRs in the original EDA. In general, there will not be a 1-to-1 correspondence between SCRs, as peak detection may miss some SCRs or detected some false peaks as SCRs, as discussed in Section 4.1.1. Thus, we compute MAE for each metric in three ways: an oracle MAE, a precision-based MAE, and a recall-based MAE.

The oracle MAE is computed assuming oracle knowledge of the s_i 's in the sampled observation model, i.e. the of the last sample prior to the onset of each SCR in $y(t)$. However, the actual SCR onset times denoted by the t_i 's are still unknown. Thus, the estimators are provided with oracle windows from which to estimate parameters rather than windows detected using peak detection on the under-sampled EDA \mathbf{y} . This oracle knowledge ensures a 1-to-1 correspondence between SCRs; however, since such oracle knowledge is not available in practice, the oracle MAE should be interpreted as a lower bound on the estimation error.

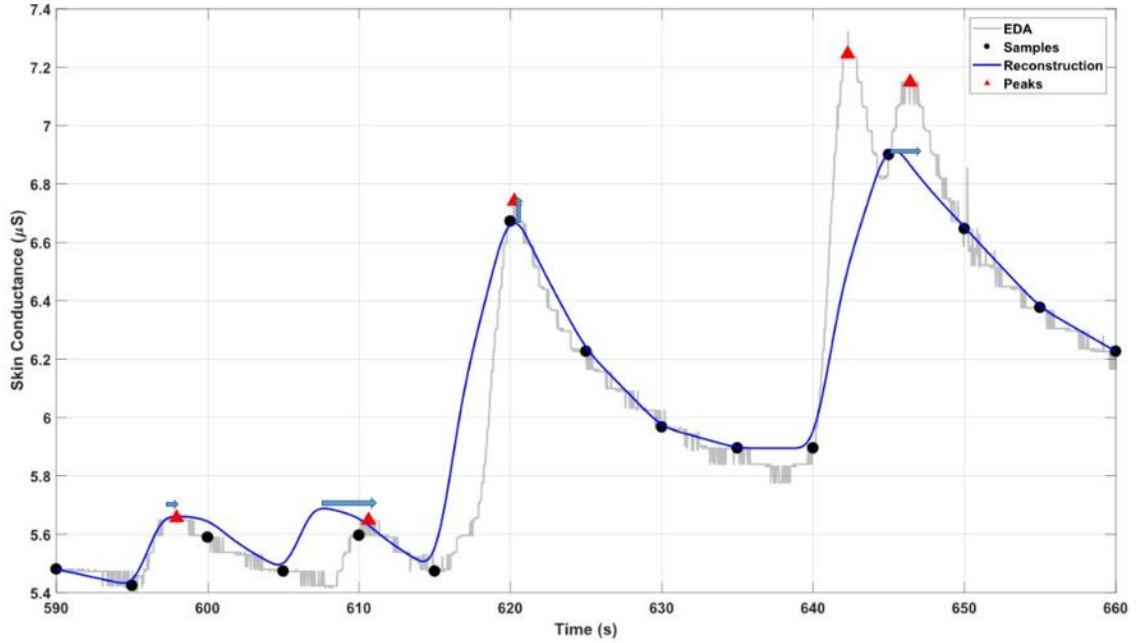


Figure 5-2: An illustration of Precision based MAE. Here we iterate through every detected peak and then try to match up the closest labeled peak.

The second metric is an extension of the ideas of precision and recall. For both of these concepts, an MAE in peak times is calculated. The precision- and recall-based MAE criteria are based on the notions of precision and recall from information retrieval. To compute the precision-based MAE, we iterate through each detected SCR and compute the MAE with respect to the nearest (in time) labeled SCR. Figure 5-2 finely illustrates the idea. As shown in 5-3 for the recall-based MAE, we iterate each labeled SCR and compute the MAE with respect to the nearest detected SCR.

Since we create 10 sub-sampled data sets from each original EDA trace, we average the MAE over all 10 data sets when reporting the results.

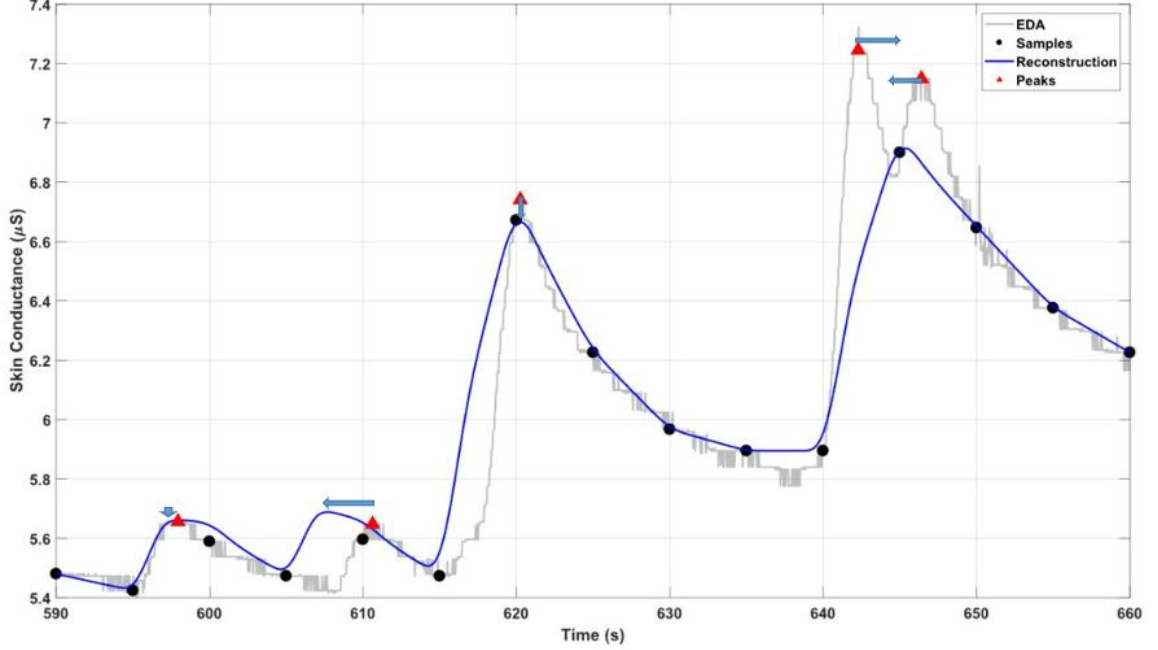


Figure 5-3: An illustration of Recall based MAE. Here we iterate through every labeled peak and then try to match up the closest detected peak.

5.1.1.3 Comparison Method: Piecewise Cubic Hermite Interpolating Polynomials

Since reconstruction of the continuous-time skin conductance $y(t)$ can be viewed as a type of structured interpolation, we compare our proposed method against a standard spline-based interpolator: a piecewise cubic Hermite interpolating polynomial (PCHIP). PCHIPs are constructed so as to be continuous with continuous first derivatives, but are not constrained to be continuous in their second derivatives as opposed to other cubic splines. This causes them to have fewer oscillations when the underlying data is less smooth than polynomials. Since the EDA data has sharp jumps corresponding to the SCRs, we favor PCHIP over standard cubic splines. Since PCHIP is based on a polynomial parametric model and also aims to minimize reconstruction error, a comparison against PCHIP evaluates the effectiveness of our proposed Bateman parametric model for overall reconstruction ability. Unlike

our MLE and MAP estimators, PCHIP does not use SCR windows, so we cannot compute any oracle MAEs, only precision- and recall-based MAEs.

5.1.2 Simulated Data

We simulate skin conductance data at 20 Hz over a duration of 5,000 seconds. We generate SCRs such that the time between SCR onsets is drawn independently from a uniform distribution between 10 and 30 seconds, so that SCRs have differing amounts of overlap. For each SCR i , we sample the SCR parameters $\alpha_i, \delta_i, \tau_{1i}, \tau_{2i}$ from the prior distributions described in Section 4.1.3.2. We treat the baseline $b(t)$ as a constant sampled from a $\Gamma(2, 2)$ distribution and assume the observation noise $n(t)$ is white Gaussian noise with variance 10^{-4} .

Since we know the actual onset times as well as the SCR parameters for each SCR, we can also calculate the peak times of each SCR by setting the derivative of (3.5) with respect to t to 0. The other 3 evaluation metrics are easily computed from the simulated data given the onset and peak times.

5.1.3 Real Data

We use a data set collected by Silveira et al. [30] using an Affectiva Q sensor with a sampling rate of 32 Hz. The Q sensor was worn on the palm and did not require any wired connections or conductive gel, so the data collected using the Q sensor should be representative of the type of data that would be collected using a consumer-grade wearable, except at a much higher sampling rate. The data used in the experiments was collected from 9 individuals (6 male, 3 female) aged between 20 to 50 years. The participants were monitored in isolation while they were being exposed to a series of short stimuli. The experiment consisted of a 220-second video clip containing 7 isolated image, audio, and video stimuli. In between each stimulus, silent intervals

were inserted where neither images nor audio were exposed to the participant.

5.1.3.1 Annotation of SCRs

Unlike with the simulated data experiment, we do not know the actual SCR onset times, so we create labels by human annotation. The labeling process was performed consistent with guidelines on EDA in the Handbook of psychophysiology [11]. Based on these guidelines and observations about frequency of SCR occurrences from other prior work [6], we employ 3 main criteria for labeling SCRs:

1. The SCR must have a faster rise than decay.
2. The SCR amplitude must be at least $0.1 \mu\text{S}$.
3. There must be at least a 3-second gap between consecutive SCRs.

We annotate the SCR onset and the peak times on the original 32 Hz EDA trace. From these annotations, we can compute the other 3 evaluation metrics.

Chapter 6

Results

6.1 Simulated Data Experiment

We report skin conductance reconstruction results at $f_d = 20$ Hz from under-sampled data at $f_s = 0.2$ Hz (sampling period $T = 5$ seconds). The oracle evaluation metrics are shown in Table 6.1, and the precision- and recall-based metrics are shown in Table 6.2.

Compared to the MLE, the MAP reconstruction more accurately preserves all SCR features in each evaluation category except for peak time in the oracle evaluation. In particular, the MLE is very inaccurate at estimating SCR amplitudes and tends to overfit by estimating SCRs with large amplitudes and short half-recovery times. This can be seen from the scatter plots of observed (actual) and reconstructed SCR features in Fig. 6-1a, where the amplitudes of many SCRs reconstructed using the MLE far exceed their observed values. On the other hand, Fig. 6-1b shows that the MAP reconstruction appears to accurately estimate amplitudes and half-recovery times, with a slight under-estimation of rise times. The use of priors has reduced the tendency of the MLE to overfit, particularly for SCR amplitudes, although there are still some cases where amplitudes are over-estimated.

The MAP reconstruction also compares favorably to PCHIP in most evaluation

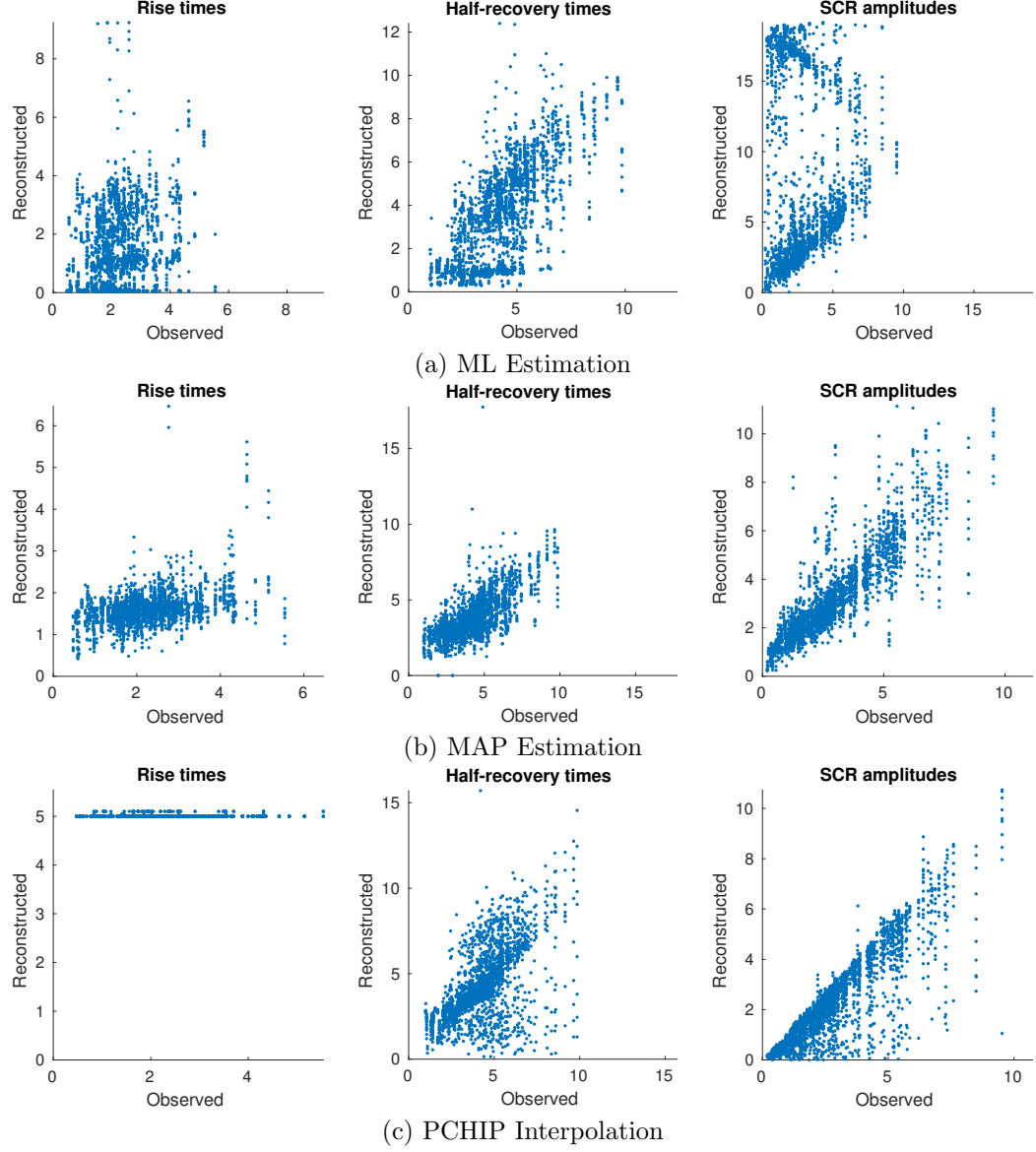


Figure 6-1: Scatter plots of observed (actual) and recovered SCR features by (a) ML estimation, (b) MAP estimation, and (c) PCHIP interpolation in simulated data experiment. Observed and recovered SCRs are matched using the precision-based approach.

Table 6.1: Oracle mean-absolute error metrics (\pm standard error) for SCR features over $N = 2,530$ SCRs in simulation experiment. Best metric within 1 standard error shown in bold.

| Parameter | MLE | MAP |
|--------------------|-----------------------------------|-----------------------------------|
| Peak time | 1.07 ± 0.02 | 1.18 ± 0.02 |
| Rise time | 1.14 ± 0.02 | 0.78 ± 0.01 |
| Half-recovery time | 1.03 ± 0.02 | 0.66 ± 0.01 |
| Amplitude | 3.24 ± 0.11 | 0.64 ± 0.01 |

Table 6.2: Precision- and recall-based mean-absolute error metrics (\pm standard error) for SCR features in simulation experiment. $N = 2,420$ SCRs for precision-based metrics for all methods, and $N = 2,530$ SCRs for recall-based metrics for all methods. Best metric within 1 standard error in each category shown in bold.

| Parameter | Precision-based | | | Recall-based | | |
|--------------------|-----------------|-----------------------------------|-----------------------------------|-----------------|-----------------------------------|-----------------------------------|
| | MLE | MAP | PCHIP | MLE | MAP | PCHIP |
| Peak time | 1.47 ± 0.03 | 1.30 ± 0.02 | 1.44 ± 0.02 | 2.01 ± 0.06 | 1.84 ± 0.06 | 1.96 ± 0.06 |
| Rise time | 1.35 ± 0.02 | 0.81 ± 0.01 | 2.75 ± 0.02 | 1.37 ± 0.02 | 0.83 ± 0.01 | 2.74 ± 0.02 |
| Half-recovery time | 1.44 ± 0.02 | 0.94 ± 0.02 | 1.06 ± 0.03 | 1.53 ± 0.03 | 1.05 ± 0.02 | 1.19 ± 0.03 |
| Amplitude | 4.54 ± 0.12 | 0.65 ± 0.02 | 0.63 ± 0.02 | 4.60 ± 0.12 | 0.77 ± 0.02 | 0.72 ± 0.02 |

categories. PCHIP interpolation results in SCRs with very high rise time. The scatter plots in Fig. 6-1c show that PCHIP estimates all rise times to be around 5 seconds, which is the sampling period. Thus, PCHIP interpolation loses the rapid rise present in SCRs. PCHIP does a better job of estimating half-recovery times and amplitudes, with a tendency to slightly under-estimate both.

6.2 Real Data Experiment

We report skin conductance reconstruction results at the original data sampling rate of $f_d = 32$ Hz from under-sampled data at $f_s = 0.2$ Hz. The data set contains 9 users in total. We show the downsampled and original EDA trace along with MLE, MAP, and PCHIP reconstructions for 2 users in Fig. 6-2 the reconstruction comparisons for the rest of the users are shown in the appendix. Similar to the simulated data experiment, we see severe over-estimates of SCR amplitude by the MLE, which provides an inferior reconstruction compared to MAP and PCHIP. These

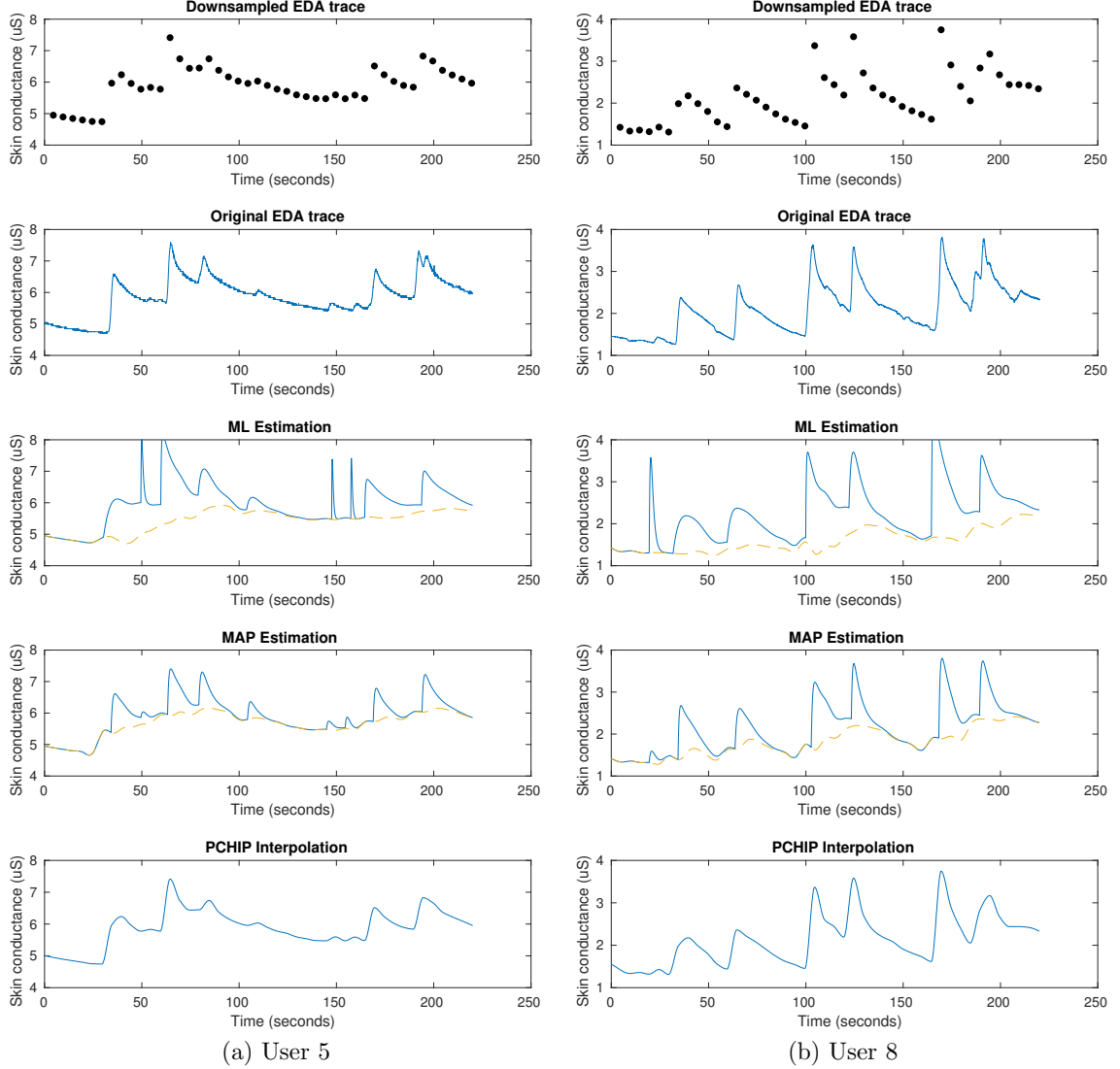


Figure 6-2: Comparison of skin conductance recovery methods on data from two users in the real data experiment. For ML and MAP estimation, the yellow dashed line denotes the estimated SCL component (PCHIP does not separate the SCL). The ML estimate has overfit, resulting in severe over-estimates of the amplitudes for several SCRs. The MAP estimate retains the shape of SCRs (fast rise and slow decay) in the original EDA trace better than the PCHIP interpolation.

Table 6.3: Oracle mean-absolute error metrics (\pm standard error) for SCR features over $N = 790$ SCRs in real data experiment. Best metric within 1 standard error shown in bold.

| Parameter | MLE | MAP |
|--------------------|-----------------------------------|-----------------------------------|
| Peak time | 2.40 ± 0.09 | 2.48 ± 0.07 |
| Rise time | 2.28 ± 0.07 | 1.34 ± 0.06 |
| Half-recovery time | 2.08 ± 0.08 | 3.07 ± 0.26 |
| Amplitude | 1.86 ± 0.14 | 0.25 ± 0.01 |

over-estimates are also reflected in the oracle metrics in Table 6.3, the precision- and recall-based metrics in Table 6.4, and the scatter plots in Fig. 6-3. Due to the smaller dynamic range in this data set and the MLE’s tendency to over-estimate amplitudes, we use a $\Gamma(2, 1)$ prior for α_i in the MAP estimate, which has a smaller prior mean. The MAP reconstructions in Fig. 6-2 demonstrate that the prior has mostly suppressed the over-estimation of SCR amplitudes.

The PCHIP reconstruction preserves the overall shape of the original data well, as one might expect from a general-purpose interpolator. However, it loses the shape of SCRs, particularly the rapid rise. This is clearly visible in the first SCR at around $t = 40$ seconds for both users, for which PCHIP over-estimates the rise time and under-estimates the amplitude. PCHIP’s over-estimation of rise times is clearly visible in Fig. 6-3c, and the over-estimation is even worse than in the simulated data experiment. On the other hand, the MAP reconstruction using the Bateman form has preserved both the rise times and amplitudes. The metrics in Tables 6.3 and 6.4 show that MAP performs quite well compared to PCHIP, particularly in rise time. Whereas PCHIP tends to slightly under-estimate SCR amplitudes, MAP tends to slightly over-estimate them, which is inherited from the sum-of-squared errors component (the MLE objective function) in the posterior probability density (4.7).

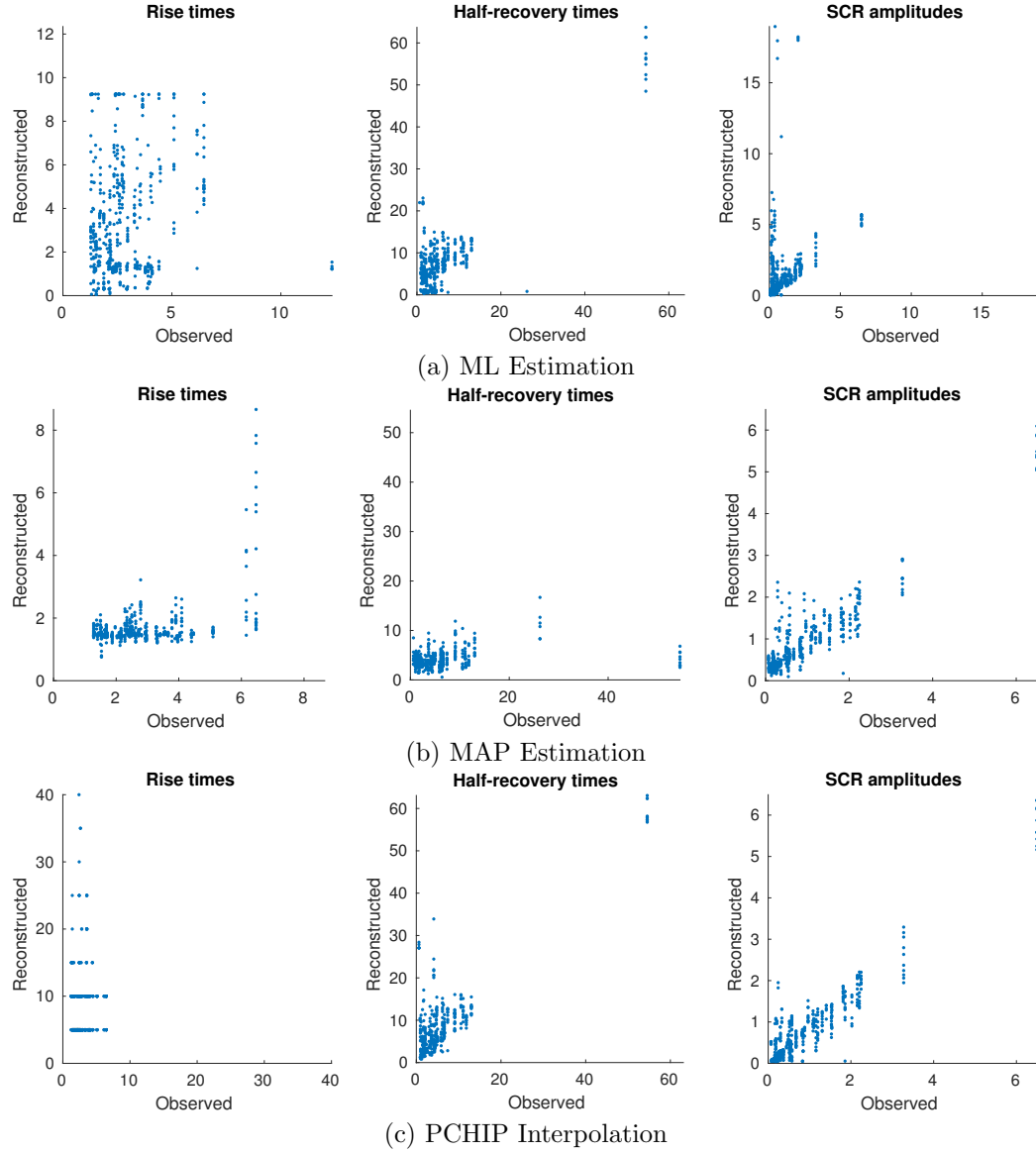


Figure 6-3: Scatter plots of observed (actual) and recovered SCR features by (a) ML estimation, (b) MAP estimation, and (c) PCHIP interpolation in real data experiment. Observed and recovered SCRs are matched using the precision-based approach.

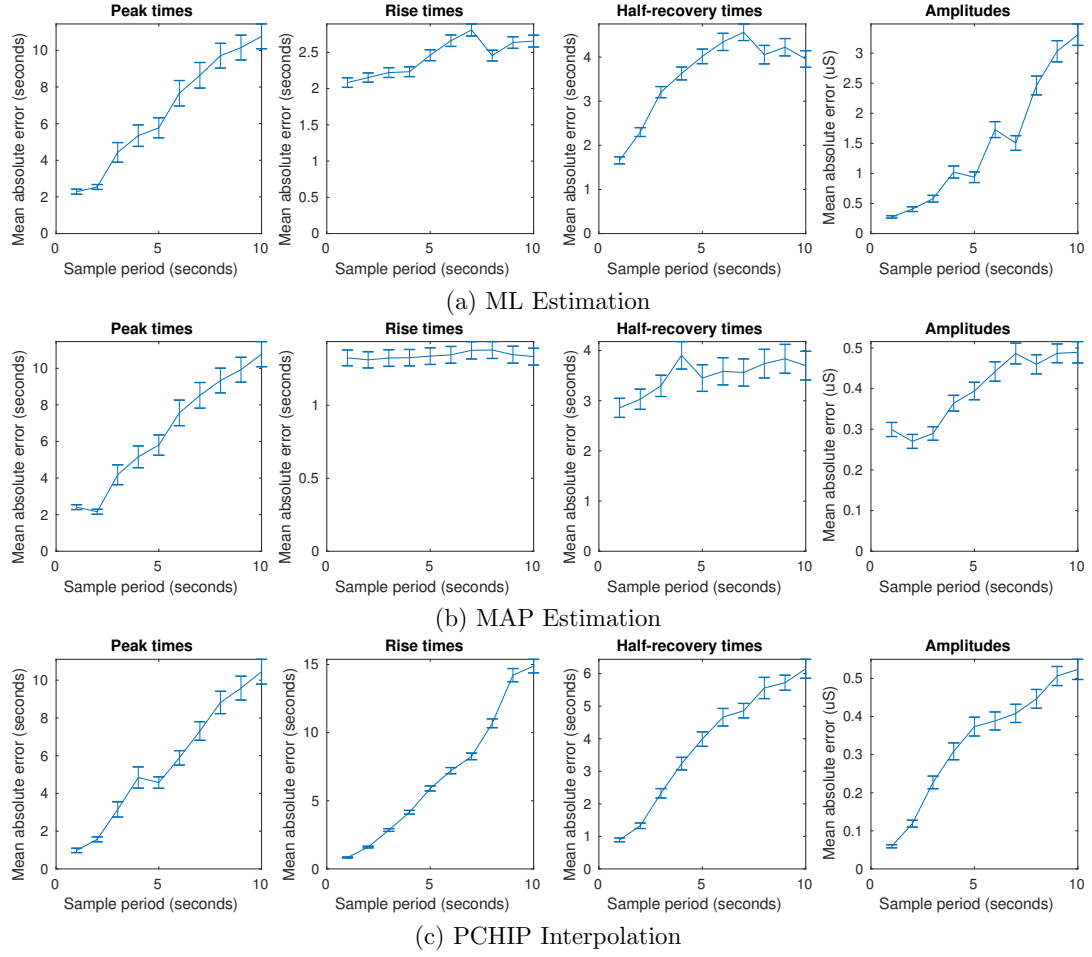


Figure 6-4: Recall-based error metrics for (a) ML estimation, (b) MAP estimation, and (c) PCHIP interpolation as sample period is varied. Error bars indicate 1 standard error. Errors in peak times and amplitudes increase roughly linearly for all methods, but the MAP estimator's errors in rise time and half-recovery time estimation increase very slowly due to the effects of the parametric form and the priors.

Table 6.4: Precision- and recall-based mean-absolute error metrics (\pm standard error) for SCR features in real data experiment. $N = 537$ SCRs for precision-based metrics for MLE and MAP, $N = 542$ SCRs for precision-based metrics for PCHIP, and $N = 790$ SCRs for recall-based metrics for all methods. Best metric within 1 standard error in each category shown in bold.

| Parameter | Precision-based | | | Recall-based | | |
|--------------------|-----------------------------------|-----------------------------------|-----------------------------------|-----------------|-----------------------------------|-----------------------------------|
| | MLE | MAP | PCHIP | MLE | MAP | PCHIP |
| Peak time | 2.93 ± 0.25 | 2.82 ± 0.25 | 2.37 ± 0.25 | 5.77 ± 0.55 | 5.81 ± 0.56 | 4.58 ± 0.30 |
| Rise time | 2.21 ± 0.08 | 1.22 ± 0.05 | 5.02 ± 0.20 | 2.46 ± 0.08 | 1.34 ± 0.06 | 5.90 ± 0.19 |
| Half-recovery time | 3.31 ± 0.15 | 3.56 ± 0.32 | 3.13 ± 0.21 | 4.02 ± 0.16 | 3.45 ± 0.27 | 3.99 ± 0.22 |
| Amplitude | 0.78 ± 0.09 | 0.28 ± 0.01 | 0.24 ± 0.01 | 0.94 ± 0.09 | 0.39 ± 0.02 | 0.37 ± 0.02 |

6.2.1 Effects of Sampling Rate

We repeat the experiment with the sample period varied from 1 second to 10 seconds to determine how the different methods and metrics are affected by the sampling rate. Since the number of detected SCRs decreases as we decrease sampling rate, we use recall-based metrics in this portion of the experiment. The variation in recall-based error metrics for each algorithm is shown in Fig. 6-4. Notice that most of the error metrics appear to increase linearly as the sample period is increased, including all of the error metrics for PCHIP. On the other hand, only the peak time increases linearly for MAP, with rise time barely increasing at all as sample period increases. This result suggests that the assumed parametric form and priors are effective for estimating SCR shapes even in a severely under-sampled setting.

Chapter 7

Conclusion

7.1 Conclusion

This thesis details the development of a statistical method in order to reconstruct EDA from under-sampled data. This method utilizes the functional form of EDA as bi-exponential functions informed by physiological knowledge. This knowledge manifests itself as priors on the parameters of the functional form so as to shift to them to more frequent values as well as constraints on the parameters in order to generate a physically consistent solution.

We applied the proposed skin conductance reconstruction methods to a simulated and a real data set, both sampled at 0.2 Hz. We compared our methods to PCHIP, a general-purpose spline-based interpolator, and found that our proposed MAP estimator more accurately preserved most of the important SCR features, particularly rise time.

We have demonstrated that it is indeed possible to accurately recover SCRs even when EDA data is collected at extremely low sampling rates necessitated by the wearable form factor. A limitation of the proposed approach includes its dependence on peak detection on the under-sampled data as a first step, which may lead to many missed peaks. It is likely that a more rigorous hypothesis testing approach could

further improve accuracy of reconstructions.

Another interesting approach would be to develop methods for real-time estimation, which would allow for adaptive sampling rates to trade off battery life and accuracy. Methods dependent on Adaptive sampling which can vary their sampling frequencies based on the context of the work that the user is believed to be in engaged in can be considered to be as viable alternatives to the above methodology. A similar alternative is to regulate the sampling interval based on the rate at which SCRs are occurring in a certain time frame. If there are very close SCRs the sampling rate can be increased to capture all the evoked SCRs and if the response of a particular user in the previous time window has been sparsely populated by skin conductance events then the sampling rate can be kept at a lower value for the future time windows.

Since its probably the very first attempt to detect Skin Conductance response changes at such low sampling frequencies this is probably a new direction to the field since we have shown that analysis of Skin Conductance Responses is possible at severe low sampling frequencies. Efficient algorithms can be developed using the statistical models developed here which can be deployed in hand held devices, wrist watches and other wearable resulting in significant battery saving and their round the clock use without the need for regular charging. Although for regular deployment and installation of the system some changes might be necessary. For example, an application which can detect motion artifacts at these sampling rates added on top of the model might make the system more robust by negating the False positives.

Bibliography

- [1] D. M. Alexander, C. Trengove, P. Johnston, T. Cooper, J. August, and E. Gordon. Separating individual skin conductance responses in a short interstimulus-interval paradigm. *Journal of neuroscience methods*, 146(1):116–123, 2005.
- [2] D. R. Bach, J. Daunizeau, K. J. Friston, and R. J. Dolan. Dynamic causal modelling of anticipatory skin conductance responses. *Biological Psychology*, 85(1):163 – 170, 2010. ISSN 0301-0511. doi: <https://doi.org/10.1016/j.biopsycho.2010.06.007>. URL <http://www.sciencedirect.com/science/article/pii/S0301051110001791>.
- [3] D. R. Bach, K. J. Friston, and R. J. Dolan. Analytic measures for quantification of arousal from spontaneous skin conductance fluctuations. *International Journal of Psychophysiology*, 76:52–55, 2010.
- [4] M. Benedek and C. Kaernbach. Decomposition of skin conductance data by means of nonnegative deconvolution. *Psychophysiology*, 47(4):647–658, 2010. ISSN 1469-8986. doi: 10.1111/j.1469-8986.2009.00972.x. URL <http://dx.doi.org/10.1111/j.1469-8986.2009.00972.x>.
- [5] M. Benedek and C. Kaernbach. A continuous measure of phasic electrodermal activity. *Journal of Neuroscience Methods*, 190(1):80–91, 2010. ISSN 0165-0270. doi: <https://doi.org/10.1016/j.jneumeth.2010.04.028>. URL <http://www.sciencedirect.com/science/article/pii/S0165027010002335>.
- [6] W. Boucsein. *Electrodermal activity: Second edition*. Springer US, 08 2013. doi: 10.1007/978-1-4614-1126-0.

- [7] J. Braithwaite, D. Watson, J. Robert, and R. Mickey. A guide for analysing electrodermal activity (eda) & skin conductance responses (scrs) for psychological experiments. Report, University of Birmingham, 2013.
- [8] J. T. Cacioppo, L. G. Tassinary, and G. G. Berntson. *Handbook of Psychophysiology*. Cambridge University Press, 3 edition, 2007. doi: 10.1017/CBO9780511546396.
- [9] T. Chaspari, A. Tsiartas, L. I. Stein, S. A. Cermak, and S. S. Narayanan. Sparse representation of electrodermal activity with knowledge-driven dictionaries. *IEEE Transactions on Biomedical Engineering*, 62(3):960–971, 2015. doi: 10.1109/TBME.2014.2376960. URL <http://ieeexplore.ieee.org/lpdocs/epic03/wrapper.htm?arnumber=6975079>.
- [10] A. Choi and H. Shin. Photoplethysmography sampling frequency: pilot assessment of how low can we go to analyze pulse rate variability with reliability? *Physiological Measurement*, 38(3):586, 2017. URL <http://stacks.iop.org/0967-3334/38/i=3/a=586>.
- [11] M. E. Dawson, A. M. Schell, and D. L. Filion. The electrodermal system. *Handbook of psychophysiology*, 2:200–223, 2007.
- [12] R. Edelberg. *Electrodermal Mechanisms: A Critique of the Two-Effector Hypothesis and a Proposed Replacement*, pages 7–29. Springer US, Boston, MA, 1993. ISBN 978-1-4615-2864-7.
- [13] S. for Psychophysiological Research Ad Hoc Committee on Electrodermal Measures. Publication recommendations for electrodermal measurements. *Psychophysiology*, 49(8):1017–1034, 2012. ISSN 1469-8986. doi: 10.1111/j.1469-8986.2012.01384.x. URL <http://dx.doi.org/10.1111/j.1469-8986.2012.01384.x>.

- [14] M. Garbarino, M. Lai, D. Bender, R. W. Picard, and S. Tognetti. Empatica e3 - a wearable wireless multi-sensor device for real-time computerized biofeedback and data acquisition. In *MobiHealth*, 2014.
- [15] A. Greco, G. Valenza, A. Lanata, E. P. Scilingo, and L. Citi. cvxeda: A convex optimization approach to electrodermal activity processing. *IEEE Transactions on Biomedical Engineering*, 63(4):797–804, 2016.
- [16] J. Hernandez, R. Morris, and R. Picard. Call center stress recognition with person-specific models. *Proc. Int. Conf. Affect. Comput. Intell. Interact.*, pages 125–134, 2011.
- [17] S. Jain, U. Oswal, K. S. Xu, B. Eriksson, and J. Haupt. A compressed sensing based decomposition of electrodermal activity signals. *IEEE Transactions on Biomedical Engineering*, In press, 2016. doi: 10.1109/TBME.2016.2632523. URL <http://arxiv.org/abs/1602.07754> <http://ieeexplore.ieee.org/document/7755834/>.
- [18] A. Krause, M. Ihmig, E. Rankin, D. Leong, S. Gupta, D. Siewiorek, A. Smailagic, M. Deisher, and U. Sengupta. Trading off prediction accuracy and power consumption for context-aware wearable computing. *2012 16th International Symposium on Wearable Computers*, 0:20–26, 10 2005. doi: 10.1109/ISWC.2005.52.
- [19] A. Krause, M. Ihmig, E. Rankin, D. Leong, S. Gupta, D. Siewiorek, A. Smailagic, M. Deisher, and U. Sengupta. Trading off prediction accuracy and power consumption for context-aware wearable computing. *Proceedings - International Symposium on Wearable Computers, ISWC*, 2005: 20–26, 2005. ISSN 0769524192. doi: 10.1109/ISWC.2005.52. URL <https://ieeexplore.ieee.org/document/1550781/>.

- [20] W. Lian, V. Rao, B. Eriksson, and L. Carin. Modeling correlated arrival events with latent semi-markov processes. In *Proceedings of the 31st International Conference on Machine Learning (ICML-14)*, pages 396–404, 2014.
- [21] C. Lim, R. Barry, E. Gordon, A. Sawant, C. Rennie, and C. Yiannikas. The relationship between quantified eeg and skin conductance level. *International Journal of Psychophysiology*, 21(2):151 – 162, 1996. ISSN 0167-8760. doi: [http://dx.doi.org/10.1016/0167-8760\(95\)00049-6](http://dx.doi.org/10.1016/0167-8760(95)00049-6). URL <http://www.sciencedirect.com/science/article/pii/0167876095000496>.
- [22] C. L. Lim, C. Rennie, R. J. Barry, H. Bahramali, I. Lazzaro, B. Manor, and E. Gordon. Decomposing skin conductance into tonic and phasic components. *International Journal of Psychophysiology*, 25(2):97 – 109, 1997. ISSN 0167-8760. doi: [http://dx.doi.org/10.1016/S0167-8760\(96\)00713-1](http://dx.doi.org/10.1016/S0167-8760(96)00713-1). URL <http://www.sciencedirect.com/science/article/pii/S0167876096007131>.
- [23] H. Lu, D. Fraundorfer, M. Rabbi, M. S. Mast, G. T. Chittaranjan, A. T. Campbell, D. Gatica-Perez, and T. Choudhury. Stresssense: Detecting stress in unconstrained acoustic environments using smartphones. In *Proceedings of the 2012 ACM Conference on Ubiquitous Computing*, pages 351–360. ACM, 2012.
- [24] R. G. Lyons. *Understanding Digital Signal Processing*. Addison-Wesley Longman Publishing Co., Inc., Boston, MA, USA, 1st edition, 1996. ISBN 0201634678.
- [25] Microsoft. Microsoft band sdk documentation. Report, Microsoft, 2015. URL <http://developer.microsoftband.com/Content/docs/Microsoft%20Band%20SDK.pdf>.
- [26] K. P. Murphy. *Machine Learning: A Probabilistic Perspective*. The MIT Press, 2012. ISBN 0262018020, 9780262018029.
- [27] A. Natarajan, K. S. Xu, and B. Eriksson. Detecting divisions of the autonomic

- nervous system using wearables. In *Proc. 38th Annu. Int. Conf. IEEE Eng. Med. Biol. Soc.*, pages 5761–5764, 2016.
- [28] V. P. Rachim, Y. Jiang, H.-S. Lee, and W.-Y. Chung. Demonstration of long-distance hazard-free wearable eeg monitoring system using mobile phone visible light communication. *Opt. Express*, 25(2):713–719, Jan 2017. doi: 10.1364/OE.25.000713. URL <http://www.opticsexpress.org/abstract.cfm?URI=oe-25-2-713>.
- [29] A. Raine, P. Venables, and M. Williams. Relationships between central and autonomic measures of arousal at age 15 years and criminality at age 24 years. *Archives of General Psychiatry*, 47(11):1003–1007, 1990. doi: 10.1001/archpsyc.1990.01810230019003. URL <http://dx.doi.org/10.1001/archpsyc.1990.01810230019003>.
- [30] F. Silveira, B. Eriksson, A. Sheth, and A. Sheppard. Predicting audience responses to movie content from electro-dermal activity signals. In *Proceedings of the ACM International Joint Conference on Pervasive and Ubiquitous Computing*, pages 707–716. ACM Press, 2013. doi: 10.1145/2493432.2493508. URL <http://dl.acm.org/citation.cfm?doid=2493432.2493508>.
- [31] J. Slak and G. Kosec. Detection of heart rate variability from a wearable differential ecg device. In *2016 39th International Convention on Information and Communication Technology, Electronics and Microelectronics (MIPRO)*, pages 430–435, May 2016. doi: 10.1109/MIPRO.2016.7522182.
- [32] H. Storm, A. Fremming, S. Oedegaard, Ø. G. Martinsen, and L. Moerkrid. The development of a software program for analyzing spontaneous and externally elicited skin conductance changes in infants and adults. *Clinical Neurophysiology*, 111(10):1889–1898, 2000.

- [33] S. Taylor, N. Jaques, W. Chen, S. Fedor, A. Sano, and R. Picard. Automatic identification of artifacts in electrodermal activity data. In *Proceedings of the 37th Annual International Conference of the IEEE Engineering in Medicine and Biology Society*, pages 1934–1937, 2015. ISBN 978-1-4244-9271-8. doi: 10.1109/EMBC.2015.7318762.
- [34] P. H. Venables and M. J. Christie. Electrodermal activity. *Techniques in psychophysiology*, 54(3), 1980.
- [35] Y. Zhang, M. Haghdan, and K. S. Xu. Unsupervised motion artifact detection in wrist-measured electrodermal activity data. In *Proceedings of the 21st ACM International Symposium on Wearable Computers*, pages 54–57, 2017.

Appendix A

Reconstruction Comparisons

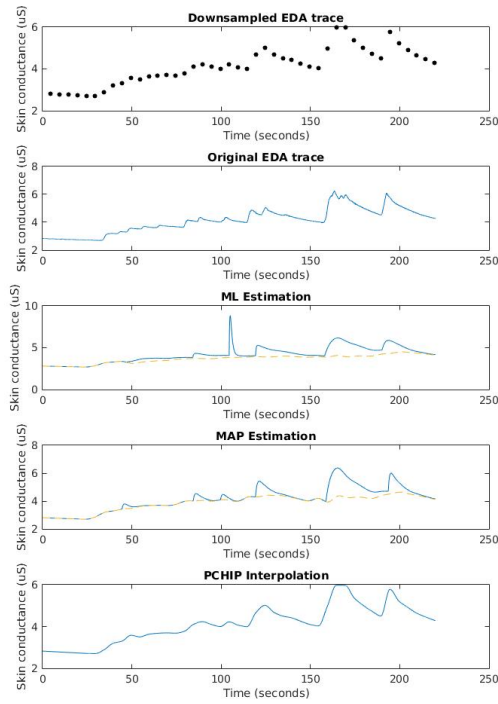


Figure A-1: Comparison of the various methods of reconstructions for user1.

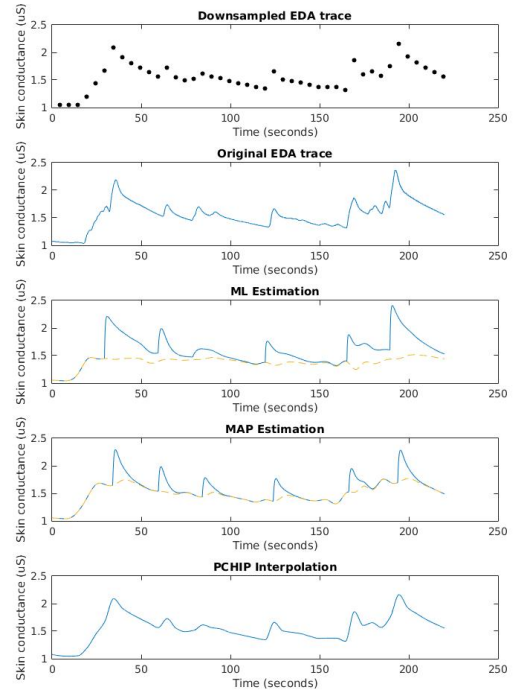


Figure A-2: Comparison of the various methods of reconstruction for user2.

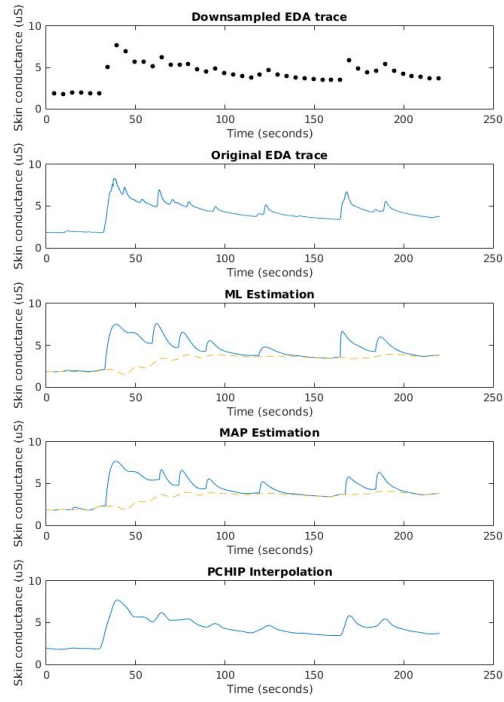


Figure A-3: Comparison of the various methods of reconstruction for user3.

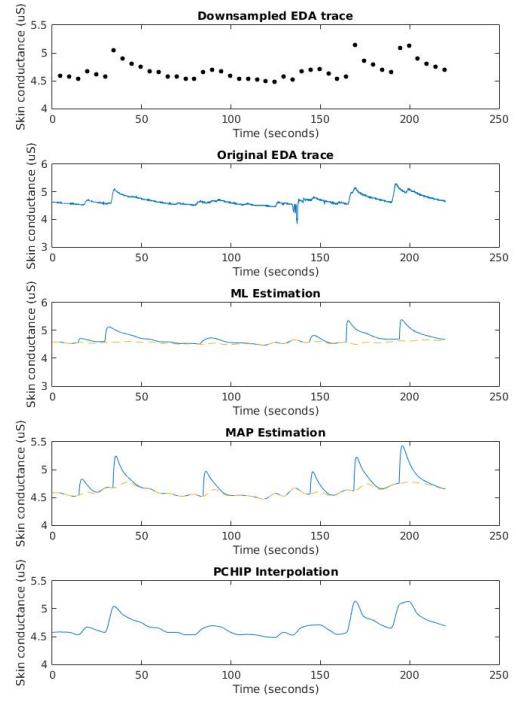


Figure A-4: Comparison of the various methods of reconstruction for user4.

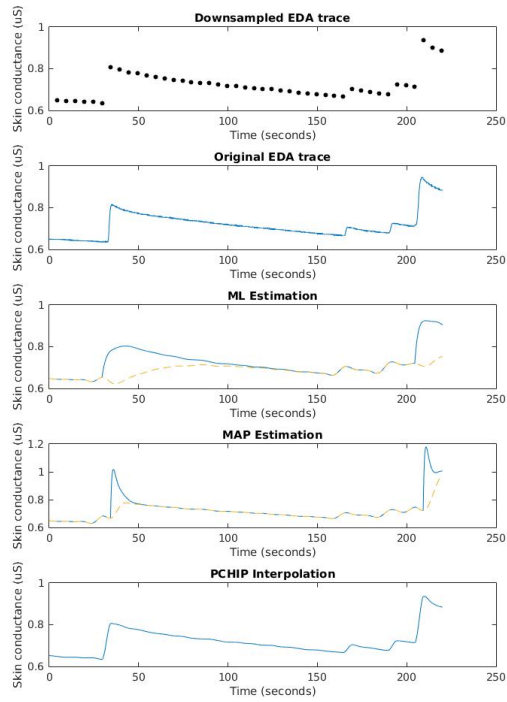


Figure A-5: Comparison of the various methods of reconstruction for user6.

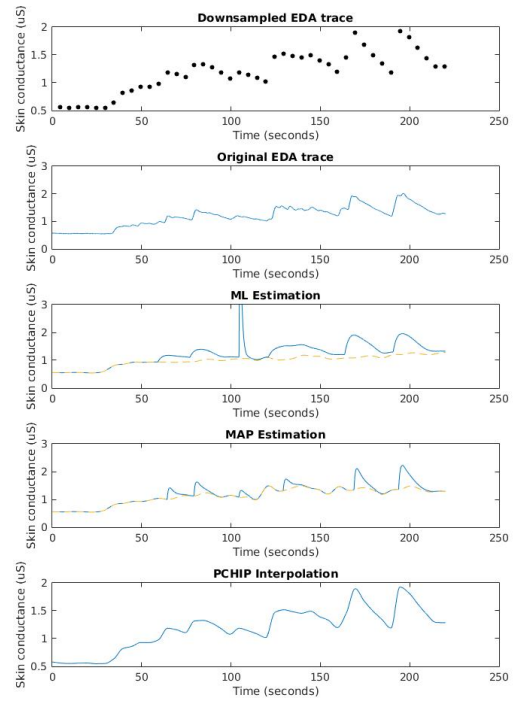


Figure A-6: Comparison of the various methods of reconstruction for user7.

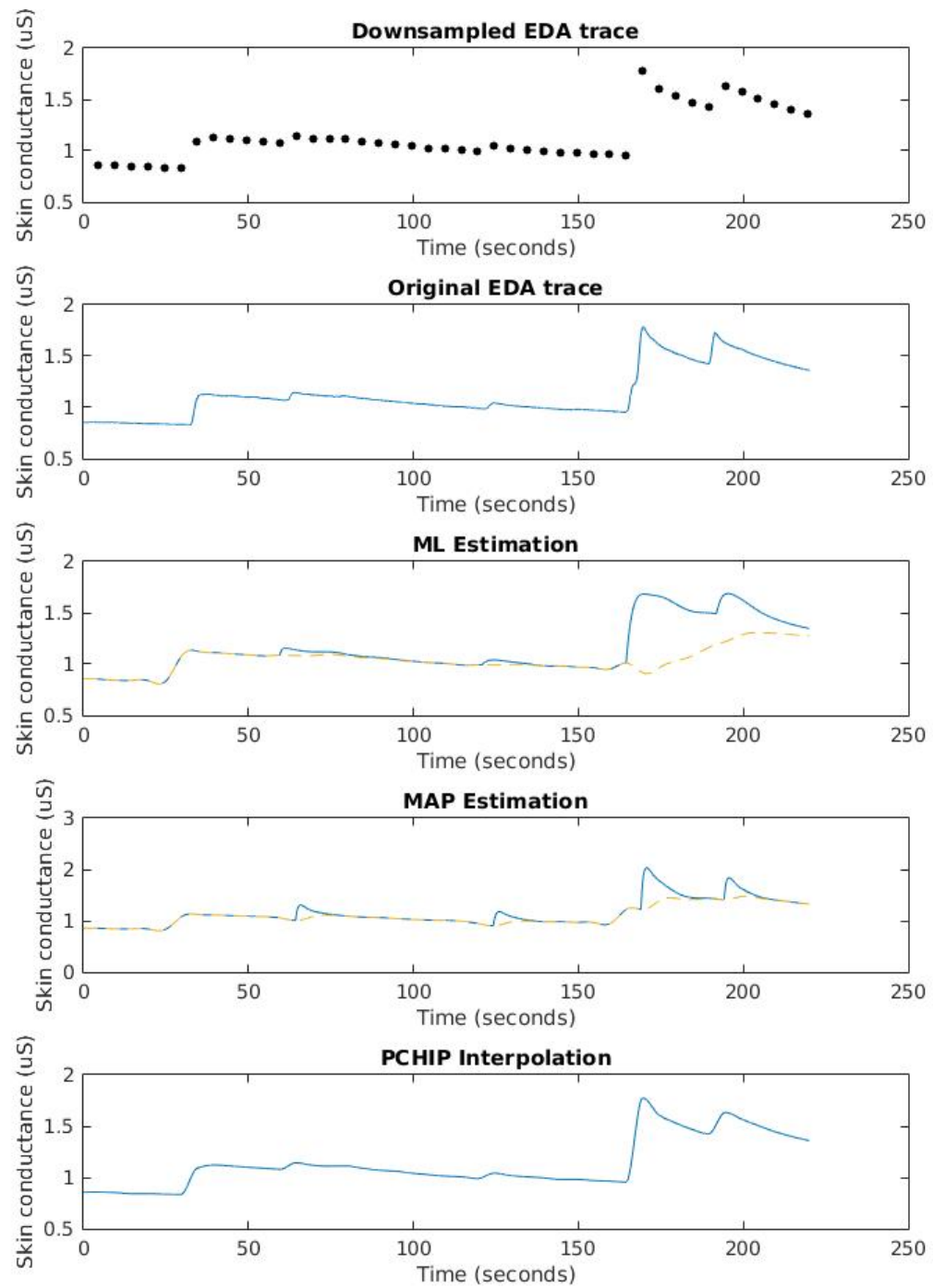


Figure A-7: Comparison of the various methods of reconstruction for user9.